Energy Conversion and Management 299 (2024) 117871

Contents lists available at ScienceDirect

Energy Conversion and Management

journal homepage: www.elsevier.com/locate/enconman

Energy management and performance analysis of an off-grid integrated hydrogen energy utilization system

Banghua Du [a], Shihao Zhu [b], Wenchao Zhu [a,b], Xinyu Lu [b], Yang Li [c], Changjun Xie [a,b,*], Bo Zhao [d], Leiqi Zhang [d], Guizhi Xu [e], Jie Song [e]

[a] Hubei Key Laboratory of Advanced Technology for Automotive Components, Wuhan University of Technology, Wuhan 430070, China
[b] School of Automation, Wuhan University of Technology, Wuhan 430070, China
[c] Department of Electrical Engineering, Chalmers University of Technology, Gothenburg 41258, Sweden
[d] State Grid Zhejiang Electric Power Research Institute, Hangzhou 310014, China
[e] State Grid Smart Grid Research Institute Co. Ltd, Beijing 102209, China

ARTICLE INFO

Keywords:
Integrated hydrogen energy utilization system
Proton exchange membrane electrolyzer
Proton exchange membrane fuel cell
Off-grid system

ABSTRACT

In integrated hydrogen energy utilization systems, due to the low efficiency of hydrogen/electricity conversion, coordination of energy management and efficient waste heat recovery is required to optimize performance. To address this challenge, this paper presents a comprehensive and sophisticated modeling and energy management strategy to enhance the off-grid energy utilization rate while prolonging the main components' lifetime. The developed model incorporates multiphase flow and heat transport balance for electricity and heat production, enabling a highly accurate representation of real-world behaviors of the system. The proposed off-grid operation strategy is complemented by a designed heat recovery scheme, ensuring the use of energy resources and waste heat. In addition, the proposed energy management strategy monitors the real-time status of each subsystem, actively reducing the number of harmful start-stop cycles of the hydrogen production system, thereby mitigating short-term power impacts and delaying its aging. Specifically, the voltage degradation of the reduction cell is reduced from 4.67 mV to 4.48 mV, the energy utilization rate is increased from 47.6 % to 53.9 %, and the energy efficiency of fuel cells significantly increases from 53.6 % to 78.1 %.

1. Introduction

Rapid decarbonization of energy systems is a core pathway to limit global temperature rise within 2 ℃ above pre-industrial levels[1,2]. Achieving this goal necessitates a shift away from fossil fuels towards renewable energy sources [3–5]. Notably, solar and wind energy have experienced remarkable growth, emerging as the fastest-increasing contributors to electricity generation since the beginning of the century. With this growth, renewables are expected to reach 40 % of total electricity generation by 2040 [2]. In this sustainable energy transition process, hydrogen has become an important energy carrier to facilitate renewable utilization due to its high energy density and ease of storage and transportation [6–8]. Hydrogen holds immense potential across various energy development and utilization scenarios, and more importantly, it has been widely recognized as one of the most environmentally friendly energy forms on the planet [9].

In recent years, many researchers have explored the hydrogen production feasibility from wind and solar photovoltaic (PV) power generation. For example, He et al. [10] examined the potential and viability of utilizing wind resources for hydrogen production in the context of environment-friendly vehicles in Pakistan. Xiao et al. [11] established a wind-hydrogen coupling system model and explored the influence of electrolyzer power and hydrogen price on the cost of hydrogen production by wind energy production. Wang et al. [12] established a decentralized robust optimization model considering the uncertainty of wind power generation and demand response to maximize the benefit of the wind-hydrogen combined system. Li et al. [13] verified the economic feasibility and limit reduction ability of the wind-PV-electrolysis-battery system, and their results show that hydrogen sales could offset the cost of electrolysis, hydrogen storage, and battery pack. Tan et al. [14] proposed a multi-time scale optimization strategy for rural electric-hydrogen-gas coupled systems while accounting for equipment uncertainty and response characteristics, facilitating effective coordination and optimization of diverse resource types to achieve its optimal allocation. Seepana et al. [15] analyzed the hydrogen

* Corresponding author at: Hubei Key Laboratory of Advanced Technology for Automotive Components, Wuhan University of Technology, Wuhan 430070, China.
E-mail address: jackxie@whut.edu.cn (C. Xie).

https://doi.org/10.1016/j.enconman.2023.117871
Received 11 August 2023; Received in revised form 19 October 2023; Accepted 8 November 2023
Available online 16 November 2023

Nomenclature

Subscripts

p	Photocurrent
EL	PEMEL
FC	PEMFC
act	Activation polarization
con	Concentration difference
ohm	Ohmic resistance
an	Anode
ca	Cathode
max	Maximum
c	Convection
r	Radiation
st	Stack
ref	Reference
tot	Total
ele	Electricity
w	Water
cond	Heat conduction
conv	Heat convection
amb	Ambient
ph	Physics
ch	Chemistry
q	Heat
dest	Destruction
sys	System
aux	Auxiliary
re	Recycle
com	Compressor
1	Condition (1)
2	Condition (2)
3	Condition (3)
4	Condition (4)
en	Energy

Symbols

N_i	Amount of substance, mol
R	Gas constant, 8.314 J/(mol•K)
T	Temperature, ℃ or K
F	Faraday's constant, 96,485C/mol
a	Activity, dimensionless
i	Current density, A/cm^2
i_0	Exchange current density, A/cm^2
F_i	Molar flow rate, mol/s
H_i	Molar enthalpy, J/mol
$\dot{Q}$	Heat exchange rate, J/s
h	Heat transfer coefficient, W/(m^2•K)
A	Area, cm^2
G	Gibbs free energy, 236.483 kJ/mol
S	Entropy, −164.025 J/(mol•K)
H	Enthalpy, 285.5 kJ/mol
Ex	Exergy, J
ex	Standard chemical exergy, J

Greek Symbols

α	Charge-transfer coefficient
ε	Emittance
σ	Stefan-Boltzmann constant, W/(m^2•K^4)
Δ	Variation
ξ	Empirical coefficient
τ	Time constant
χ	Component ratio

production potential of PV power plants in different regions of India and the feasibility of developing various optimal configurations at different locations.

Most of the above studies are microgrid or hydrogen-electric coupling systems containing hydrogen energy, and there are few designs and studies on the comprehensive utilization system of hydrogen energy considering the waste heat. The comprehensive utilization system of hydrogen energy has the advantages of simple structure and low cost [16], which has considerable development prospects. Since the operation mode and other factors of hydrogen energy equipment have a great impact on its efficiency, life, and other performance indicators, it is necessary to optimize the operation strategy of the hydrogen energy system. In the study of hydrogen energy systems, Dong et al. [17] proposed an improved scene tree algorithm to achieve energy cost savings, offering higher robustness than the traditional scene tree algorithm. Liu et al. [18] proposed a distributed multi-energy system based on hydrogen, which can coordinate the supply and demand relationship of hydrogen, electricity, cold, heat, and other energy media to achieve the best economic benefits. Babatunde et al. [19] compared the operating costs of different system structures in different regions. They concluded that adding a hydrogen energy storage system would reduce the related capital cost, thus increasing the economic feasibility of a hydrogen energy storage system. Ishaq et al. [20] analyzed and compared the energy efficiency of hydrogen production in three ways: Solar PV, geothermal power generation, and biomass gasification, and investigated the system behavior and the influence on the system efficiency through a parameter analysis of the system. Large heat generation in each component is inevitable in a hydrogen energy integrated utilization system due to relatively low energy conversion efficiency. It is promising to recover this substantial amount of energy to increase the energy utilization rate, but unfortunately, insufficient efforts have been made in this research area.

Hydrogen production and consumption are the two energy conversion processes in an integrated hydrogen energy system. The most mature technique for hydrogen production is water electrolysis, and the hydrogen consumption is mostly attributed to fuel cells. In water electrolysis, electricity is consumed by a water electrolyzer to decompose water into oxygen and hydrogen. The three main types of electrolyzers are alkaline electrolyzers, proton exchange membrane electrolyzers (PEMEL), and solid oxide electrolyzers, amongst which the PEMEL has the salient advantages of low environmental impact, high purity of hydrogen output, and fast response to power fluctuation [21–23]. PEMEL can constantly produce hydrogen under a stable electricity supply but at the expense of high electricity consumption costs. This technical and economic problem can be overcome by combining renewable energy with water electrolysis hydrogen production [24]. Existing studies have proven that frequent start-stop, power fluctuations, and high-frequency current ripple will expedite the dissolution, inactivation, agglomeration, and passivation of PEMEL electrocatalysts, as well as exacerbate the degradation of membranes and metal ion poisoning [25,26]. Chandesris et al. [27] explored the impact of temperature and current density on membrane aging by studying fluoride emissions during PEMEL operation. Frensch et al. [28] compared the performance and aging of PEMEL over time under seven different operating conditions and deduced that dynamic operation would lead to increased passivation of the catalyst carrier. Weiß et al. [29,30] proposed an accelerated stress test (AST) method for PEMELs that imitates fluctuating power sources and verified the negative impacts of frequent start-stop, power fluctuations, and prolonged PEMEL life for high-power operation. Therefore, reducing the number of electrolyzer starts should

also be considered in the energy management strategy to slow down the aging and prolong the lifetime of the electrolyzer. Compared to electrolyzers, fuel cells have been more intensively studied. The current commercialized fuel cell technologies include proton exchange membrane fuel cells (PEMFC), solid oxide fuel cells, and direct methanol fuel cells, amongst which the PEMFC possesses the advantages of high proton conductivity (0.1 S/cm^{-1} at 120 ℃), excellent thermal and chemical stability, high mechanical strength, and better durability [31,32]. Researchers are more concerned with efficient and stable operation (ESO) of PEMFC system. For example, Li et al. [33–35] proposed a hierarchical performance enhancement control strategy (HPECS), a model predictive control (MPC)-based energy management strategy (EMS) combining self-trending prediction and the subset-searching algorithm and a real-time EMS for multi-stack fuel cell hybrid system, which can effectively improve the performance, anti-disturbance ability and tracking ability of the system, reduce the operating cost, and make the PEMFC system efficient and stable operate. Therefore, the ESO of PEMFC should also be considered when designing the EMS.

In view of the above, we notice that the current research on the integrated hydrogen energy utilization system focuses on hydrogen-electric hybrid energy storage, with little involvement in the operation mode and waste heat recovery means. The off-grid operation mode and the effect of power fluctuations and frequent start-stop on the electrolyzer's lifespan are also commonly neglected for microgrid applications. This study, therefore, contributes to developing an integrated hydrogen energy utilization system under off-grid operation conditions based on multiphase flow balance. The main work and contributions of this study are as follows:

1) An energy management strategy is proposed to ensure that each subsystem can work normally, so that the electrolyzer can avoid frequent start and stop operation, so as to prolong its service life.

2) The BiLSTM network is used to predict the demand power of the fuel cell and control it through the feedback of the PID controller, which can quickly track the power shortage signal of the grid and realize the timely power compensation function.

3) The temperature sensor detects the working temperature of the electrolyzer and the fuel cell. When it exceeds the set value, the cooling water cooling system starts to work. The heat exchange plate exchanges heat with the cooling water to maintain the working temperature, and the waste heat is recovered and utilized.

The rest of this paper is structured as follows. Section 2 derives the mathematical models of the integrated hydrogen energy utilization system based on multiphase flow equilibrium. Section 3 describes the operating principles and proposes a control strategy for energy management. Section 4 presents key metrics for evaluating the system in terms of energy efficiency, and voltage degradation to verify that the proposed control strategy can extend the life of the electrolyzer and improve energy utilization. Section 5 verifies the feasibility of the developed model and analyzes the simulation results corresponding to the relevant metrics. Conclusions are drawn in Section 6.

2. System description and model development

This section proposes an integrated hydrogen energy utilization system, as shown in Fig. 1, based on which the development of its mathematical model is presented.

In the proposed system, the PV panels and wind turbine system produce electricity to supply the microgrid load. In the off-grid operating mode, the system must provide sufficient power to meet the electricity demand, even when renewable energy sources are unavailable. Integrating a hydrogen-based energy storage system brings greater flexibility by storing excess energy during high renewable generation periods and compensating for insufficient power supply during low renewable energy periods. The electrolyzer system consists of PEMEL and auxiliary devices such as water pumps, water tanks, and heating filaments, and it uses surplus electricity to produce hydrogen. On the other hand, the fuel cell system consists of PEMFC and auxiliary devices such as air compressors and humidifiers, and it uses hydrogen to generate electricity. In addition, the heat generated during hydrogen production and consumption is captured to warm water, which can be

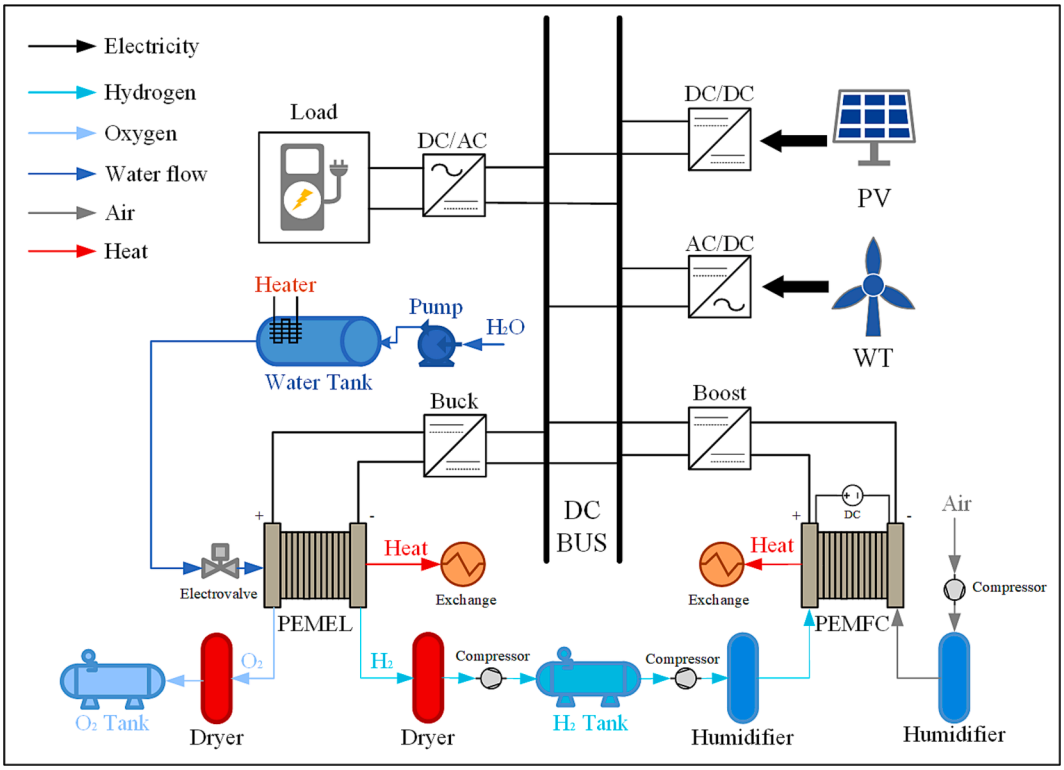

Fig. 1. System configuration.

repurposed for secondary use, thereby enhancing the overall energy utilization of the process.

2.1. Renewable energy generation subsystem

The renewable energy subsystem mainly comprises the PV and wind power generation systems. The PV system power output is obtained by establishing the current versus voltage (*I-V*) characteristic and considering the effect of solar irradiance and temperature. The wind turbine characteristic curve and wind speed data are used to describe the action of the wind turbine.

2.1.1. PV array model

In the PV system, the electric potential is established through the absorption of photons and excitation of charge in the p-region and n-region. The core component of the PV system is the solar cell, which is physically similar to a p-n junction diode. In the process of current conduction, optoelectronic devices are not ideal. They are subject to the influence of the resistances generated by material and particle conduction losses, equivalently represented by a series resistance R_s. Due to the inability to achieve a fully ideal design in the PV module, there is inevitably light-generated current leakage in the external circuit and internal circulation of the PV devices. This leakage current phenomenon is indicated in the equivalent circuit using a parallel leakage resistor R_{sh}. By applying Kirchhoff's current law, the *I-V* characteristic of the PV cell can be described by [36],

$$I_{PV} = I_p - I_0\left[\exp\left(\frac{V_{PV}+I_{PV}R_s}{n_{diode}V_t}\right)-1\right]-\frac{V_{PV}+I_{PV}R_s}{R_{sh}} \tag{1}$$

where I_{PV} and V_{PV} are the current and voltage of the PV cell, respectively, I_p is the photogenerated current, I_0 is the saturation current, n_{diode} is the ideal factor of the diode, and V_t is the thermal voltage. The output power of a PV system consisting of n_{PV} cells is calculated by

$$P_{PV} = n_{PV}V_{PV}I_{PV} \tag{2}$$

2.1.2. Wind turbine model

In the wind power generation system, a wind turbine (WT) drives a permanent magnet synchronous generator (PMSG) to produce electricity, and its output power is converted to DC power through a rectifier and a boost converter. The rectifier and boost converter ensure the power quality meets the requirements to be connected to the microgrid DC bus. The dynamics and losses in the PMSG and converters are ignored. Thus the DC output of the wind system is equal to the wind energy captured by the blades of the WT and converted into kinetic energy to drive the PMSG [37]:

$$P_{WT} = \frac{1}{2}\rho_{air}\pi r_{WT}^2 v_{wind}^3 C_{p,WT}(\lambda,\theta) \tag{3}$$

where ρ_{air} is the air density, v_{wind} is the wind speed, r_{WT} is the rotor blade radius, and the rotor efficiency $C_{p,WT}$ is a function of the tip speed ratio (λ) and the pitch angle (θ).

2.2. Electrolyzer subsystem

In this section, the nonlinear behaviors of the PEMEL are modeled using electrochemical, thermodynamic, and zero-dimensional hydrodynamic principles. The following assumptions on operating conditions were made for establishing the PEMEL model:

- The anode and cathode ends are fully saturated with water vapor;
- Water cannot be compressed;
- The gas/liquid phase can be separated;
- No evaporation of water to dissipate heat during the reaction process.

2.2.1. Electrochemical model of the PEMEL stack

The cell voltage of a PEMEL working is the current model can be calculated by [38]

$$V_{cell,EL} = E_{oc} + V_{act} + V_{con} + V_{ohm} \tag{4}$$

where E_{oc} is the open-circuit voltage, V_{act} is the activation overpotential, V_{con} is the concentration overpotential, and V_{ohm} is the ohmic overpotential. They are given by [39]

$$\begin{cases} E_{oc} = E_0 + \dfrac{RT_{EL}}{2F}\left[\ln\left(p_{H_2}p_{O_2}^{0.5}\right)\right] \\ \eta_{act} = \dfrac{2RT_{EL}}{F}\operatorname{arcsinh}\left(\dfrac{i_{EL}}{2i_{0,an}}\right)+\dfrac{2RT_{EL}}{F}\operatorname{arcsinh}\left(\dfrac{i_{EL}}{2i_{0,ca}}\right) \\ \eta_{con} = -\dfrac{RT_{EL}}{nF}\ln\left(1-\dfrac{i_{EL}}{i_{max}}\right) \\ \eta_{ohm} = I_{EL}\cdot R_{ohm} \end{cases} \tag{5}$$

where $E_0 = 1.229 - 0.9 \times 10^{-3}(T_{EL} - T_{ref})$, R is the gas constant, F is Faraday's constant, and T_{EL} is the stack temperature. $I_{EL} = i_{EL}\bullet A_{EL}$ is the operating current, where i_{EL} and A_{EL} represent the current density and electrode cross-sectional area, respectively. Furthermore, $i_{0,an}$ and $i_{0,ca}$ represent the exchange current densities in the anode and cathode, respectively, i_{max} is a defined maximum current density, and R_{ohm} is the electrolyzer cell resistance. The gas pressure of hydrogen and oxygen, p_{H_2} and p_{O_2}, are calculated from the equilibrium equations of water and gas multiphase flow [40]:

Anode:

$$\begin{cases} \dfrac{dN_{O_2}}{dt} = F_{O_2,ai} - F_{O_2,ao}(p_{O_2}, p_{H_2O,a}) + \dfrac{n_{EL}I_{EL}}{4F}\eta_F = 0 \\ \dfrac{dN_{H_2O,a}}{dt} = F_{H_2O,ai} - F_{H_2O,ao}(p_{O_2}, p_{H_2O,a}) - F_{H_2O,eod} - F_{H_2O,d} = 0 \\ p_{O_2} = \dfrac{N_{O_2}RT_{EL}}{V_{an}} \end{cases} \tag{6}$$

Cathode:

$$\begin{cases} \dfrac{dN_{H_2}}{dt} = F_{H_2,ci} - F_{H_2,co} + \dfrac{n_{EL}I_{EL}}{2F}\eta_F = 0 \\ \dfrac{dN_{H_2O,c}}{dt} = F_{H_2O,ci} - F_{H_2O,co} + F_{H_2O,eod} + F_{H_2O,d} = 0 \\ p_{H_2} = \dfrac{N_{H_2}RT_{EL}}{V_{ca}} \end{cases} \tag{7}$$

Membrane:

$$F_{H_2O,eod} = \frac{n_d i_{EL}}{F}\cdot n_{EL}M_{H_2O}A_{EL} \tag{8}$$

where V_{an} and V_{ca} are the volumes of the anode and cathode, respectively. N_i and F_i represent the molar hold-up and molar flow rate of substance i, respectively. n_d is the electro-osmotic drag coefficient, n_{EL} denotes the number of cells, and M_{H_2O} is water's molecular weight. The reader is referred to [40] for the detailed expressions of different molar flux rates.

2.2.2. Thermodynamic model of the PEMEL stack

The dynamic performance of PEMEL is dependent on its temperature. The lumped capacitance method is adopted here since it has been widely adopted in the literature (see, e.g., Hug et al. [41] and Ulleberg [42]). In this method, the temperature is assumed to be uniform within the stack, which gives the thermodynamic equilibrium of the stack [43]:

$$C_P\frac{dT_{EL}}{dt} = P_{EL} + \sum(F_iH_i)_{in} - \sum(F_iH_i)_{out} - \sum\dot{Q}_{EL} \tag{9}$$

where C_P is the total heat capacity of the pile, H_i represents the molar

enthalpy of substance i, respectively. Considering the output temperature is equivalent to the electrophile temperature, and the input temperatures are equal in both the anode and cathode chambers, the steady-state equilibrium of matter facilitates the occurrence of the standard reaction enthalpy ΔrH. This gives

$$\sum (F_i H_i)_{\text{in}} - \sum (F_i H_i)_{\text{out}} = F^{\text{in}}_{\text{H}_2\text{O,ai}} \cdot C_{P,\text{H}_2\text{O}} \cdot \left(T^{\text{in}}_{\text{H}_2\text{O}} - T_{\text{EL}}\right) - \frac{I_{\text{EL}}}{2F} \cdot \Delta rH \quad (10)$$

where $F_{\text{H}_2\text{O,ai}}$ is the anode inlet water flow rate, $C_{P,\text{H}_2\text{O}}$ is the heat capacity of water, and $T^{\text{in}}_{\text{H}_2\text{O}}$ is the anode inlet water temperature.

In (9), P_{EL} is the electrical power consumed by the PEMEL, and it can be calculated considering the isolated thermo-neutral voltage U_{in} permitted by the contained power breakdown [44]:

$$P_{\text{EL}} = n_{\text{EL}} \left(V_{\text{EL,cell}} - U_{\text{in}}\right) \cdot I_{\text{EL}} + I_{\text{EL}} \cdot \frac{\Delta rH}{2F} \quad (11)$$

Substituting (10) and (11) into (9) yields a unified expression for the heat balance of the power pile, i.e.,

$$C_P \frac{dT_{\text{EL}}}{dt} = F^{\text{in}}_{\text{H}_2\text{O,ai}} \cdot C_{P,\text{H}_2\text{O}} \cdot \left(T^{\text{in}}_{\text{H}_2\text{O}} - T_{\text{EL}}\right) + \left(V_{\text{EL}} - U_{\text{in}}\right) \cdot I_{\text{EL}} - \sum \dot{Q}_{\text{EL}} \quad (12)$$

Here, the loss term $\sum \dot{Q}_{\text{EL}}$ is the sum of heat exchanges between the pile and the atmosphere/cooling circuit, calculated by

$$\sum \dot{Q}_{\text{EL}} = (h_c + h_r) \cdot A_{\text{st}} \cdot (T_{\text{EL}} - T_{\text{amb}}) \quad (13)$$

where A_{st} is the surface area of the stack, and T_{amb} is the ambient (and surrounding shell) temperature. Furthermore, h_c is the convective heat transfer coefficient obtained by an empirically determined relation for the Nusselt number [45], and h_r is the radiative heat transfer coefficient given by

$$h_r = 4\varepsilon\sigma T_m^3 \quad (14)$$

where T_m is the average temperature in Kelvin of the heap surface and closed vessel.

The parametric values of the variables of the PEMEL model are given in Table 1[394043].

2.3. PEMFC subsystem

In this section, the nonlinear characteristics of PEMFC are modeled using electrochemical, thermodynamic, and zero-dimensional hydrodynamic principles. The following assumptions on PEMFC operating conditions were made for establishing a PEMFC model:

- There is no pressure gradient at the cathode and anode, which means that only diffusion is considered without gas convection;
- There is no vacuum or suction at the inlet and outlet of the gas stream path;
- The thermal conductivity of materials used in batteries is constant;
- Only interface resistance of the diffusion layer and collector plate is considered in the cell structure;
- Disregarding anode overpotential.

Table 1
Values of parameters in PEMEL.

Parameter	Value	Parameter	Value
$V_{\text{an}}/V_{\text{ca}}$	0.005 (m^3)	$i_{0,\text{ca}}$	2×10^{-3} (A/cm^2)
$M_{\text{H}_2\text{O}}$	18 (g/mol)	C_P	61.9 (kJ/K)
A_{EL}	50 (cm^2)	U_{in}	1.48 (V)
n_{EL}	150	A_{st}	0.7546 (m^2)
$i_{\max}$	2 (A/cm^2)	h_c	14.55 [W/(m^2•K)]
T_{ref}	298 (K)	ε	0.6
T_{amb}	25 (℃)	σ	5.67×10^{-8} [W/(m^2•K^4)]
$i_{0,\text{an}}$	2×10^{-7} (A/cm^2)		

2.3.1. Electrochemical model of the PEMFC stack

Due to similar operating principles, the PEMFC model is similar to the PEMEL model as presented in Section 2.2. Due to irreversible losses, the actual cell voltage of PEMFC decreases with decreasing equilibrium potential. In addition to temperature, pressure, and current density, factors affecting electrode polarization or overpotential include electrode material, electrode surface state, and solution composition [46]. The output voltage of a PEMFC single cell can be expressed as follows [47–49]

$$V_{\text{cell,FC}} = E_{\text{oc}} - V_{\text{act}} - V_{\text{con}} - V_{\text{ohm}} \quad (15)$$

$$\begin{cases} E_{\text{oc}} = \dfrac{\Delta G}{2F} + \dfrac{\Delta S}{2F}\left(T_{\text{FC}} - T_{\text{ref}}\right) + \dfrac{RT_{\text{FC}}}{2F}\left[\ln\left(p_{\text{H}_2} p_{\text{O}_2}^{0.5}\right)\right] \\ V_{\text{act}} = \xi_1 + \xi_2 T_{\text{FC}} + \xi_3 T_{\text{FC}} \ln\left(\dfrac{p_{\text{O}_2}}{5.08 \times 10^6 \exp(-498/T_{\text{FC}})}\right) + \xi_4 T_{\text{FC}} \ln(I_{\text{FC}}) \\ V_{\text{con}} = b_1 \exp(b_2 I_{\text{FC}}) \\ V_{\text{ohm}} = I_{\text{FC}} \cdot R_{\text{ohm}} \end{cases} \quad (16)$$

where ΔG is Gibbs free energy change, ΔS is entropy change, I_{FC} is the cell current, T_{FC} is the cell temperature, b_1 and b_2 are empirical coefficients fitted by experiments. Similar to PEMEL, the gas pressure p_{H_2} and p_{O_2} as well as the molar flux rate $F_{\text{H}_2,\text{ci}}$ of the hydrogen used by the PEMFC are calculated from the equilibrium equations of water and gas multiphase flow and the reader is referred to [50] for detailed expressions. The output power of a PEMFC stack with n_{FC} cells connected in series is calculated as

$$P_{\text{FC}} = n_{\text{FC}} \cdot V_{\text{cell,FC}} \cdot I_{\text{FC}} \quad (17)$$

2.3.2. Thermodynamic model of the PEMFC stack

The PEMFC stack temperature T_{FC} (℃) significantly affects the cell performance. An increase in T_{FC} improves cell performance, but overtemperature can cause a dry membrane leading to a decrease in cell performance. Therefore maintaining a proper T_{FC} is essential to maintain its performance. Load changes will affect T_{FC}. An increase in load current increases both T_{FC} and power consumption.

The output power P_{FC} is a part of the total energy $P_{\text{tot,FC}}$ entering the fuel cell stack. Besides, a part $P_{\text{tot,FC}}$ is stored by the stack, causing a change in T_{FC}, and a small part $\dot{Q}_{\text{loss}}$ is dissipated into the air. If the stack is cooled by circulating water, another part $\dot{Q}_{\text{cool}}$ of the energy is carried away by the cooling water. When spatial variations are ignored, the energy conservation equation $\partial(\varepsilon\rho c_p T)/\partial t + \nabla\cdot(\varepsilon\rho c_p \vec{u} T) = \nabla\cdot(k^{eff}\nabla T) + S_Q$ can be used to derive a reduced equation:

$$C_t \frac{dT_{\text{FC}}}{dt} = \dot{Q}_{\text{stack,FC}} = P_{\text{tot,FC}} - P_{\text{FC}} - \dot{Q}_{\text{cool}} - \dot{Q}_{\text{loss}} \quad (18)$$

where $\dot{Q}_{\text{stack,FC}} = S_Q$ is the heat absorption power of the stack and C_t is the heat capacity.

The total power $P_{\text{tot,FC}}$ entering the stack is related to the amount of substance of hydrogen consumed by the reaction, which in turn is related to the stack current and the number of cells in the stack. The following expression can be obtained:

$$P_{\text{tot,FC}} = \dot{m}_{\text{H}_2,\text{used}} \Delta H = \frac{n_{\text{FC}} I_{\text{FC}}}{2F} \Delta H \quad (19)$$

where ΔH is the enthalpy of hydrogen and $\dot{m}_{\text{H}_2,\text{used}}$ is the reaction rate of hydrogen.

The expression for the amount of heat taken away by the cooling water is given by

$$\dot{Q}_{\text{cool}} = h_{\text{HX}} \frac{\left(T_{\text{FC}} - T_{w,\text{in}}\right) - \left(T_{\text{FC}} - T_{w,\text{out}}\right)}{\ln\left[\left(T_{\text{FC}} - T_{w,\text{in}}\right)/\left(T_{\text{FC}} - T_{w,\text{out}}\right)\right]} \quad (20)$$

where $T_{w,\text{in}}$ and $T_{w,\text{out}}$ are the temperatures of cooling water inlet and outlet, respectively, and h_{HX} can be obtained by

$$h_{\text{HX}} = h_{\text{cond}} + h_{\text{conv}} \tag{21}$$

where h_{cond} and h_{conv} are the thermal conductivity and convective heat transfer coefficient of the heat exchanger, respectively.

The heat radiated outward by the stack $\dot{Q}_{\text{loss}}$ (W) can be expressed by

$$\dot{Q}_{\text{loss}} = (T_{\text{FC}} - T_{\text{amb}})/R_t \tag{22}$$

where R_t is the thermal resistance (℃/W) is calculated by

$$R_t = \frac{\tau}{C_t} = \frac{MC}{h_A C_t} \tag{23}$$

where MC is the product of the mass and specific heat capacity of the stack, and h_A is the heat transfer coefficient of the stack.

The parametric values used in this work are given in Table 2[47–49].

2.4. Hydrogen storage subsystem

The hydrogen produced by PEMEL is stored in HST. A continuous hydrogen stream is charged into the tank until the tank pressure reaches its maximum value $p_{\text{HST\_max}}$ or there is no hydrogen flow. The HST is a subsystem where the hydrogen output from the PEMEL is fed from the HST inlet, and the hydrogen needed by the PEMFC is fed from an assumed virtual inlet. We define the state of hydrogen storage (SOH) as the mass of hydrogen stored in the tank, calculated by

$$\begin{aligned}\text{SOH} &= \frac{N_{\text{HST}}}{M_{\text{H}_2}} \\ &= \text{SOH}_0 + \frac{1}{M_{\text{H}_2}} \int_0^t \left(\underbrace{F_{\text{H}_2,\text{co}}}_{\text{Output H}_2 \text{ molar flow rate of EL}} - \underbrace{F_{\text{H}_2,\text{ci}}}_{\text{Input H}_2 \text{ mass flow rate of FC}} \right) dt\end{aligned} \tag{24}$$

where SOH_0 is the initial hydrogen mass, N_{HST} is the amount of hydrogen in the HST, and M_{H_2} is the molar mass of the hydrogen. The input and output hydrogen flow rates of the HST are calculated based on the PEMEL model and the PEMFC model presented in Section 2.2 and Section 2.3, respectively.

The hydrogen storage is limited by the designed gas tank size $\text{SOH}_{\text{max}} = 25$ kg. To calculate the lower limit of hydrogen storage, one can use the ideal gas equation:

$$p_{\text{HST}} V_{\text{HST}} = N_{\text{HST}} R T_{\text{HST}} = \text{SOH} \cdot M_{\text{H}_2} R T_{\text{HST}} \tag{25}$$

where p_{HST} is the hydrogen pressure, V_{HST} is the volume of the HST, and T_{HST} is hydrogen temperature. Thus, the pressure limits are proportional to the storage limits at given V_{HST} and T_{HST}. Considering the maximum allowable pressure $p_{\text{HST\_max}} = 25$ bar, and the hydrogen pressure in the tank must be at least atmospheric, i.e., $p_{\text{HST\_min}} = 1$ bar, one can calculate the lower storage limit $\text{SOH}_{\text{min}} = 4$ kg.

Table 2
Values of parameters in PEMFC.

Parameter	Value	Parameter	Value
ΔG	236.483 (J/mol)	n_{FC}	150
ΔS	−164.025 [J/(mol•K)]	C_t	135.1 (kJ/K)
T_{ref}	298 (K)	ΔH	285.5 (kJ/mol)
ξ_1	−0.9514	$T_{w,\text{in}}$	25 (℃)
ξ_2	0.00312	$T_{w,\text{out}}$	30 (℃)
ξ_3	7.4×10^{-5}	h_{cond}	35.55 (W/℃)
ξ_4	-1.87×10^{-4}	h_{conv}	0.025 [W/(℃•A)]
A_{FC}	150 (cm^2)	T_{amb}	25 (℃)
b_1	3×10^{-5} (V)	MC	35 (kJ/K)
b_2	8×10^{-3} (cm^2/mA)	h_A	17 (W/K)

Thus, the operating constraints for the HST are imposed as

$$4 \text{ kg} \leq \text{SOH} \leq 100 \text{ kg} \tag{26}$$

3. System operation strategy for energy management

In the previous section, the model of each subsystem is introduced. Each subsystem requires an efficient energy management strategy to coordinate its operations. Implementing such an energy management strategy entails devising corresponding control schemes tailored to the characteristics of each device. In the following, the start-stop logic of PEMEL, HST, and PEMFC will be described in detail, along with specific control schemes, aiming to optimize energy utilization and the efficiency of each subsystem.

As shown in Fig. 2, the hydrogen energy integrated utilization system collects information such as the power flows in the system and the amount of hydrogen stored in the HST. The information is sent to a supervisory controller. The start-stop signals of the electrolyzer and fuel cell are processed and delivered to determine the operation status of each subsystem. The control system of the PEMEL analyzes the average available power of the wind turbine and PV and evaluates whether it is sufficient for the hydrogen energy system. The PEMEL needs to be manually started and kept on hot standby, waiting for a hydrogen production command from the control system. The control scheme triggers the opening of the electrolyzer based on the available power and the remaining capacity of the HST. This process is shown in Fig. 3, and the decision to turn on the electrolyzer depends on all of the following conditions being met:

- The input power is set to 20 kW or higher;
- Input power will last for 50 min;
- Sufficient hydrogen storage in HST is available.

Consider the scheme mentioned as an “AND” logic gate that merges the three inputs, and each is regarded as a Boolean signal. These Boolean signals are characterized by binary representation, wherein TRUE indicates the fulfillment of the stated condition and FALSE signifies the non-fulfillment of the condition.

The first control objective is to ensure the minimum net power. This mandates that the power level maintains above a specific threshold depending on the electrolyzer’s characteristics. In this particular design, the minimum power of the PEMEL is 20 kW, equal to the rated power of the auxiliary engine. When the condition “Available Power”> “Minimum Power” is met, a Boolean output value of TRUE is assigned.

As Matute et al. [51] highlighted, it is crucial to mitigate unnecessary transitions from cold to hot standby/production to prevent the accelerated stack aging that can shorten the PEMEL’s lifetime. Although PEMEL can cope with fluctuating power inputs, frequent starts and stops of the stack can impact stack life. While the PEMEL system can effectively adapt to variable power inputs, frequent start-stop cycles of the stack can adversely impact its longevity. Consequently, the second imperative within the control system necessitates a continuous power signal instead of discrete transitions. Implementing a timer mechanism becomes imperative to curtail unnecessary “open” and “close” actions, eliminating short-duration pulses and ensuring a consistent power supply during electrolyzer operation. Periods with insufficient renewable energy reserves lead to a temporary closure of the electrolyzer, thereby mitigating costs. A dedicated “timer” subsystem facilitates the seamless operation of the electrolyzer, effectively minimizing abrupt switching frequencies. The architecture of the control system is depicted in Fig. 4.

The third requirement for electrolyzer control is to ensure a sufficient level of storage in the HST. This is because the electrolyzer does not need to produce hydrogen if HST has reached its rated capacity. The HST model contains an output signal which is then transmitted returning to the electrolyzer to notify the state of the HST. A TRUE signal indicates the HST is available for storage, and a FALSE indicates the tank is full.

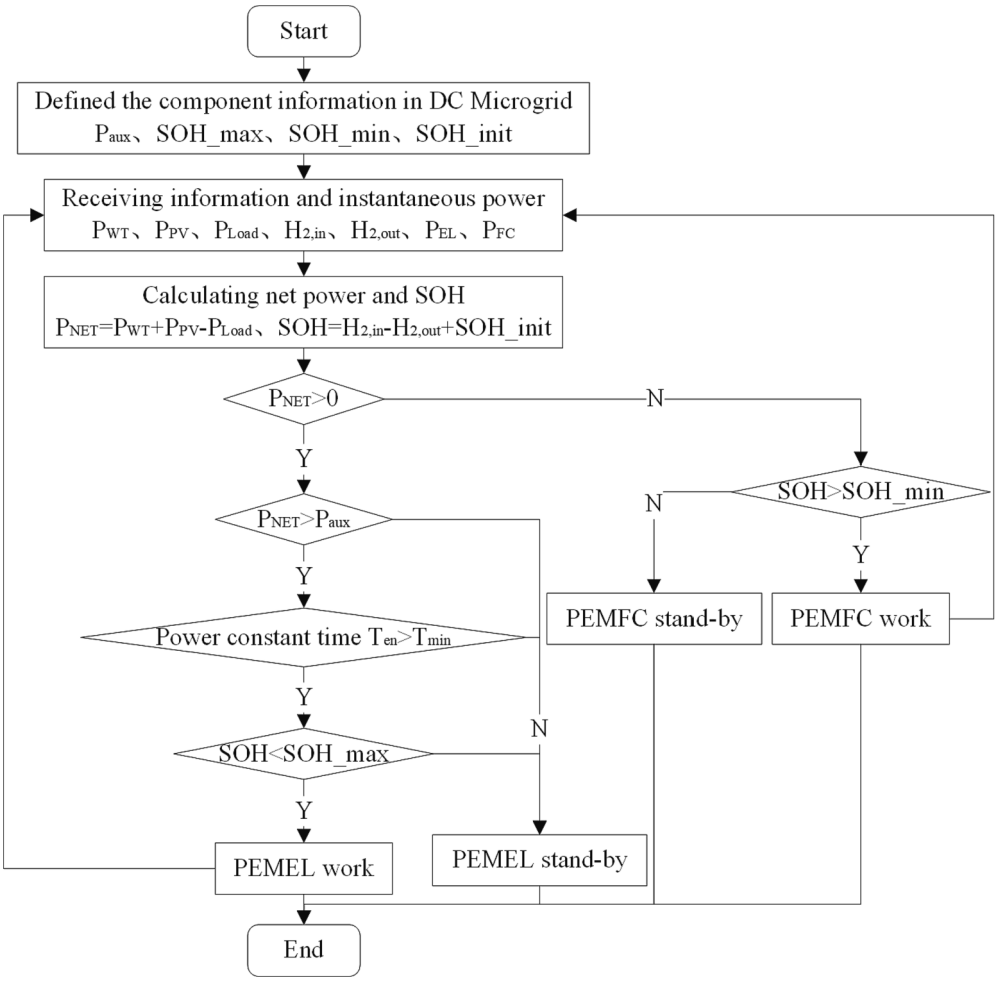

Fig. 2. Chart of system control.

The Boolean signal from the HST and the predicted available power is fed into the electrolyzer control scheme signal, which is next sent into the "with" module and the continuous minimum available Boolean signal. If all are TRUE, the power is fed to the electrolyzer, where the maximum used power of the available power is determined by the electrolyzer rating. If any signal is FALSE, the system is directed to the hot standby mode. In this study, Bi-directional Long Short-Term Memory (BiLSTM) is adopted to realize power prediction. Through the learning and training of historical data, the power fluctuations in a given period of time are predicted. BiLSTM is based on a simple LSTM network, and by adding a network layer that transmits information in reverse time order, it can further extract the features of time series data and enhance the learning ability and prediction accuracy of the model [52].

The fuel cell obtains hydrogen from the system's electricity production. Starting up a fuel cell requires a power gap based on the DC microgrid's load demand and renewable power supply. If the fuel cell rating is lower than the notch signal, the fuel cell will provide the corresponding rated power. When the power gap is low, it only provides the power of the corresponding gap. The fuel cell is started by checking two signals: A power gap signal and a signal indicating enough hydrogen in the HST. The fuel cell starts only when both signals indicate the condition is suitable for electricity generation, as shown in Fig. 5. The fuel cell needs to be warmed up to a certain value before starting to conserve energy consumption. Since the fuel cell needs to supply power through the power deficit in the grid, a feedback control scheme using PID controllers is adopted at the fuel cell inlet to regulate the air intake at the inlet to achieve the power-following effect. In the fuel cell system, the same power prediction model as the electrolyzer system is used to realize the judgment of power demand.

According to Faraday's first law, it can be shown that the amount of hydrogen involved in the reaction in the anode chamber of the PEMFC is related to the current flowing in the fuel cell as

$$N = \frac{I}{2F} \tag{27}$$

Therefore, power following can be achieved by converting the power required by the grid into a current signal so that the operating current of the fuel cell follows this demand current signal under the action of the PID controller.

Next, we propose a thermal energy management strategy. The heat generated from the operation of the electrolyzer and fuel cell operation is captured by heating cold water and then utilized to meet the thermal demands of users within the microgrid. This subsequently leads to an enhancement in the overall energy utilization of the system. The specific implementation methodology is depicted in Fig. 6. Activation of the cooling system occurs when the operating temperature of either the electrolyzer or fuel cell surpasses 80 ℃. This activation effectively maintains the temperature at this threshold. The heat extracted through this cooling mechanism is subsequently stored in the water and employed to supply the preheating of the hydrogen energy comprehensive utilization system and part of the heat load demand in the industrial park[53]. Table 3 illustrates that, in comparison to other viable heat storage materials, water enjoys a higher heat storage density per unit weight and unit volume.

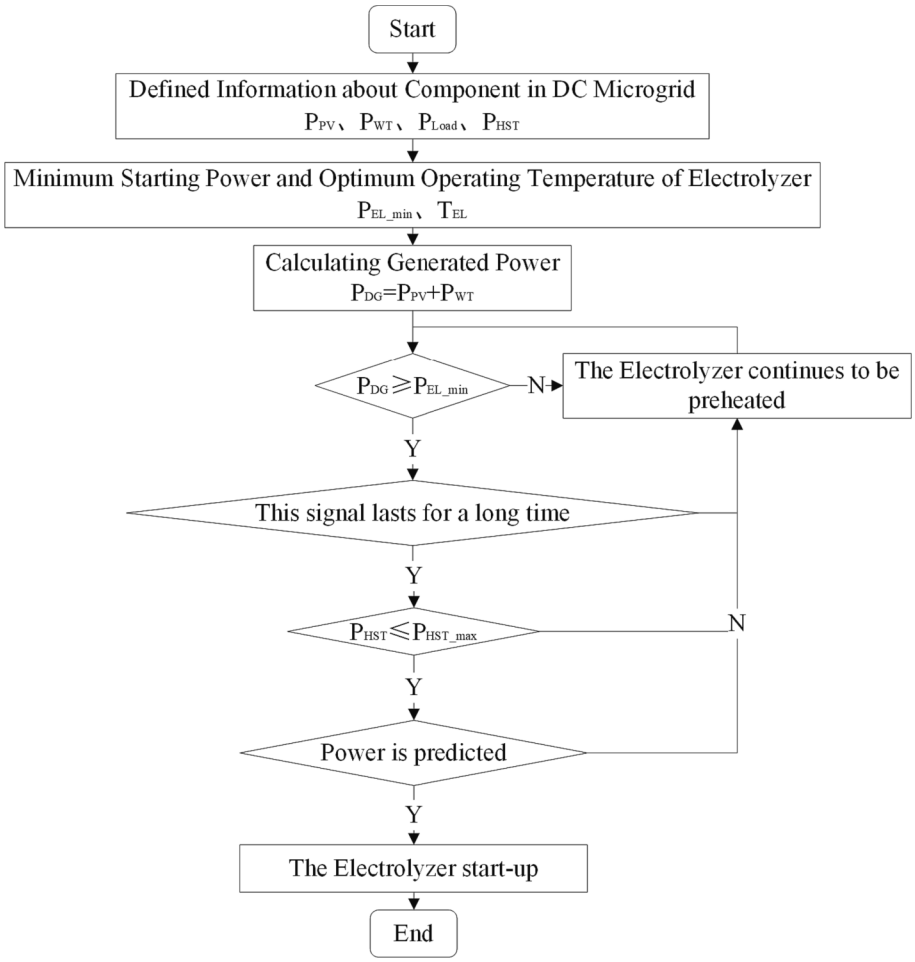

Fig. 3. Electrolyzer work logic.

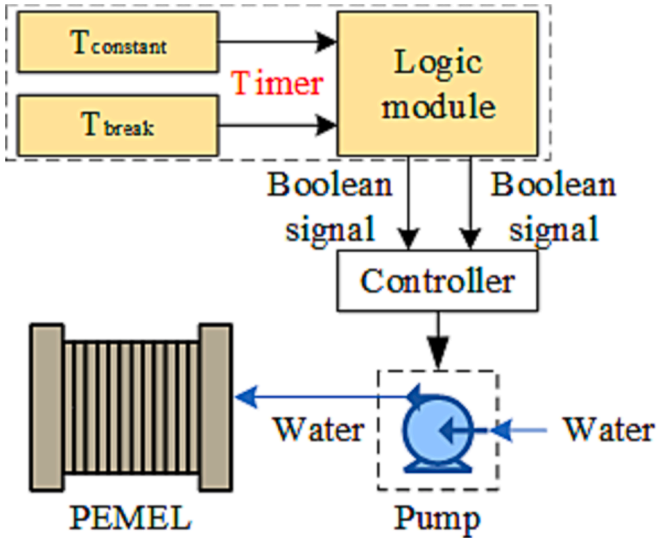

Fig. 4. Block diagram for electrolyzer continuous power timer control.

Furthermore, water has the advantages of being both pollution-free and cost-effective. It also lends itself to easy processing and storage within a temperature range spanning from 0 to 100 ℃. Consequently, water stands as a suitable choice for heat storage material. Nonetheless, directly heating water to its boiling point not only results in inefficient energy utilization but also incurs relatively high costs for high-temperature heat storage. Therefore, the stored hot water temperature is typically regulated within the range of 40 to 90 °C. Given that this study warms up the water by heat exchange, the storage water temperature is set at 60 ℃.

4. Performance analysis

The characteristics of the system components will be analyzed and evaluated in this section based on the developed model in Section 2. The following assumptions are made in the analysis:

- All systems are in a steady state;
- Changes in potential and kinetic energy are ignored;
- Operations of the turbine and pump are adiabatic;
- Losses in the heat transfer process and pressure drops in the piping are not taken into account;
- The ambient pressure p_{amb} and temperature T_{amb} are assumed to be 101.325 kPa and 25 ℃.

4.1. Aging analysis of the PEMEL system

PEMEL degradation will result in an increase in the operating voltage. The primary reason for such voltage degradation is dynamic operation, and the major failure modes and the causes are summarized in Table 4 [25,26,29,54]. The voltage degradation rate of PEMEL varies at different operating conditions, and this relationship can be employed for quantitative assessment of PEMEL aging. The frequent start-stop

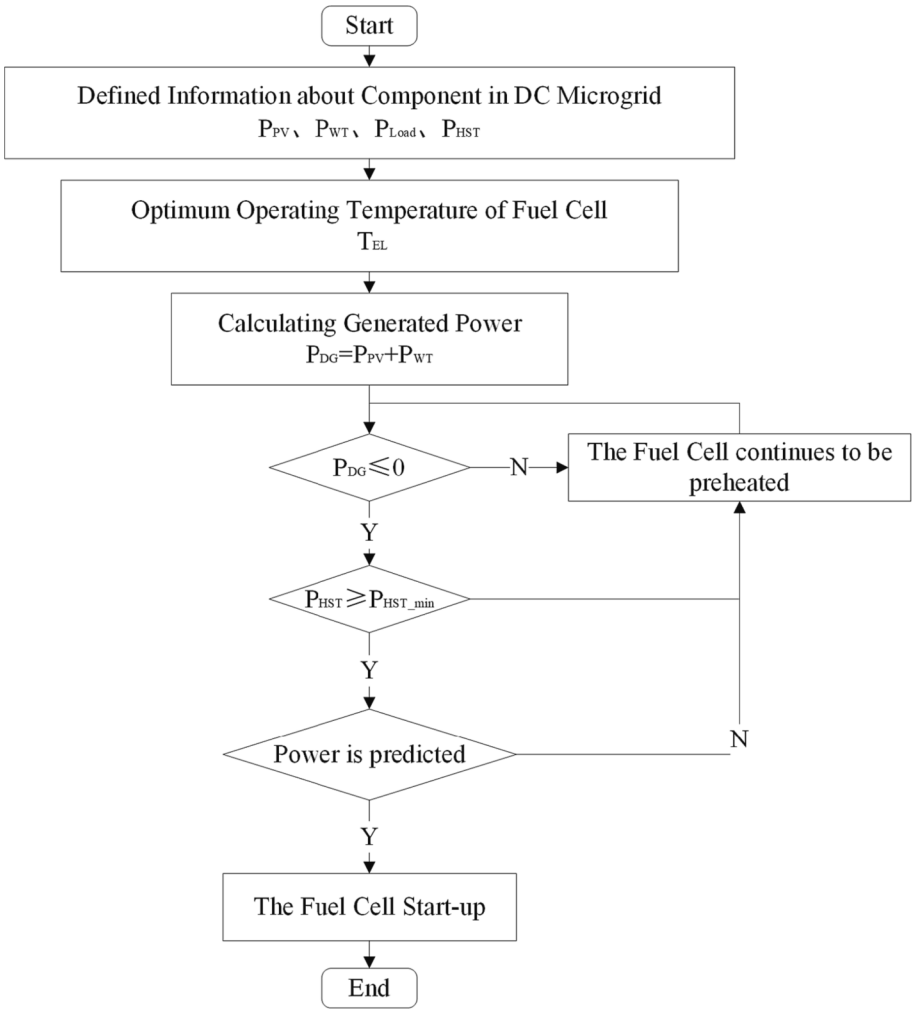

Fig. 5. Fuel cell work logic.

operations substantially impact the voltage degradation rate, reaching an extent of 230 μV/h. As the cell voltage gradually increases with the aging, the PEMEL efficiency η_{EL} operating at the same power will gradually decrease over time.

4.2. Exergy analysis of the PEMFC system

Conducting exergy analysis becomes essential for evaluating the variations in the performance capabilities of different energy forms. Exergy encompasses kinetic, potential, physical, and chemical exergy [55]. The system is considered stationary concerning the environment, rendering any changes in its kinetic and potential energies negligible.

Mass exergy is the sum of physical and chemical exergy given by

$$Ex = Ex_{ph} + Ex_{ch} \tag{28}$$

The physical and chemical exergy is the aggregate of the individual physical and chemical exergy of each constituent, i.e.,

$$Ex_{ph} = \sum F_i[(h_i - h_0) - T_{amb}(s_i - s_0)] \tag{29}$$

$$Ex_{ch} = F_{mix}\left(\sum \chi_i ex_{ch,i} + RT_{amb}\sum \chi_i \ln\chi_i\right) \tag{30}$$

where F_{mix} and F_i are the molar flow rate of the mixed fluid and component i in the mixed fluid, respectively. ex_i is the standard chemical exergy of component i, given in Table 5.

The exergy equilibrium is expressed as

$$Ex_{in} = Ex_{out} + W + Ex_q + Ex_{dest} \tag{31}$$

where Ex_{in} and Ex_{out} denote the exergy of inflow and outflow systems, respectively, W and Ex_q denote work exergy and thermal exergy, respectively, and Ex_{dest} denotes the exergy destruction. The thermal exergy can be derived from the Carnot cycle, given by

$$Ex_q = (1 - T_{amb}/T_{Heat})\cdot Q \tag{32}$$

where T_{Heat} is the temperature of the heat exchange source, and Q is the thermal energy contained in the heat exchange source.

4.3. Performance evaluation parameters of the system

The overall performance of the integrated hydrogen energy utilization system is evaluated using four indicators, including PEMEL hydrogen production energy efficiency, PEMFC integrated energy efficiency, exergy destruction, and exergy efficiency.

PEMEL hydrogen production energy efficiency is expressed as

$$\eta_{EL\_sys} = \frac{n_{H_2}\cdot HHV - W_{EL\_aux}}{W_{PV+WT}} \tag{33}$$

where W_{EL_aux} and W_{PT+WT} are the electrical energy consumed by the auxiliary devices of the electrolyzer system and the electricity produced by the renewables.

The PEMFC integrated energy efficiency is expressed as

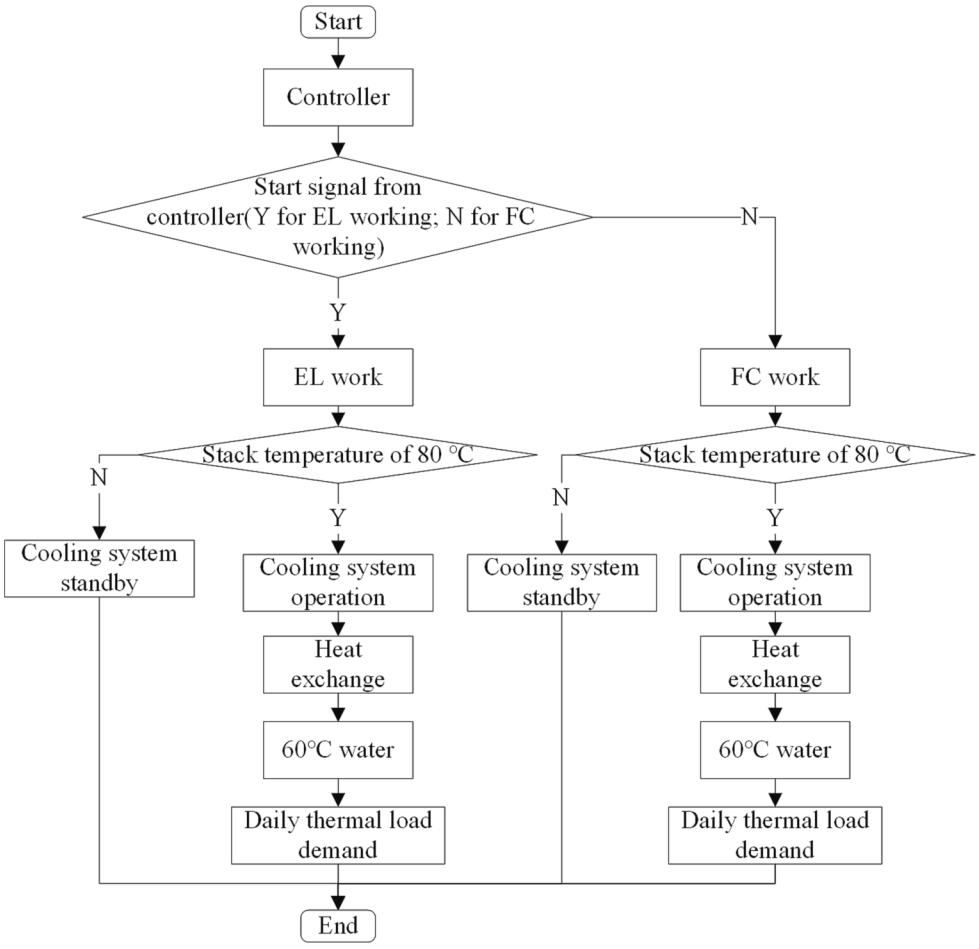

Fig. 6. Flowchart of the thermal management policy.

Table 3
Heat storage density per volume for different materials.

Material	Specific heat [kJ/(kg·K)]	Heat content per volume [MJ/(m^3·K)]
Water	4.2	4.2
Oil	2.0	1.7
Ice	2.0	1.8
Sand	0.8	1.2
Concrete	0.8	2.1
Steel	0.5	3.6

Table 4
Effect of dynamic operation on the degradation of PEMEL components.

Failure modes	Causes	Consequences
Dissolution of catalyst	Current reversal during power off	V_{act}↑
Agglomeration of catalyst	Load cycle and start-stop switch	V_{act}↑
Passivation of electrode	Frequent fluctuations in current	V_{ohm}↑
Poisoning of membrane		V_{ohm}↑

$$\eta_{FC\_sys} = \frac{W_{FC,net} - W_{FC\_aux} + Q_{re}}{n_{H_2} \cdot LHV} \tag{34}$$

where $W_{FC,net}$ and W_{FC_aux} are the electrical energy produced by the PEMFC and consumed by the auxiliary machine of the fuel cell system, and Q_{re} denotes the recovered thermal energy.

In fuel cell systems, the total exergy destruction is the summation of the exergy destruction of the components. The equations for calculating exergy destruction for individual components of the subsystem are given in Table 6. Since only the air compressor consumes power, the exergy efficiency of the fuel cell system can be expressed as

$$\eta_{FC,ex} = \frac{W_{FC,net} - W_{com}}{m_{H_2} \cdot ex_{H_2} - Q_{re}} \tag{35}$$

where m_{H_2} and ex_{H_2} denote the total mass and standard chemical exergy of hydrogen, respectively.

Table 5
Standard exergy of several substances.

Substances	Standard chemical exergy(J/mol)
N_2	693
O_2	3948
H_2	236,100
H_2O (vapor/liquid)	9500/900

Table 6
Governing equations of destruction for individual components.

Components	Exergy destruction
PEMFC	$Ex_{FC,dest} = Ex_{FC,in} - Ex_{FC,out} - W_{FC,net} - Ex_q$
Humidifier	$Ex_{hum,dest} = Ex_{hum,in} - Ex_{hum,out} - W_{hum}$
Compressor	$Ex_{com,dest} = Ex_{com,in} - Ex_{com,out} - W_{com}$
Cooling	$Ex_{cool,dest} = Ex_{cool,in} - Ex_{cool,out} + Ex_q$

5. Results and discussion

5.1. Model validation

5.1.1. Test system

The experimental data for model validation and simulation are obtained from a demonstration project of integrated hydrogen energy systems. As shown in Fig. 7, the system consists of an electrolyzer hydrogen production system, a hydrogen storage system, and a fuel cell power production system. The hydrogen production system consists of a 200-kW PEMEL stack, auxiliary engines, and heat recovery pipes. The hydrogen storage system includes three-stage (3 MPa, 20 MPa, and 45 MPa) hydrogen storage tanks, pressure-reducing valves, and compressors. The power generation system comprises a 120-kW PEMFC stack, auxiliary devices, and heat recovery pipes.

5.1.2. Validation of the PEMEL model

Simulations were conducted to verify the developed PEMEL model by comparing the output characteristics. In the simulation, the membrane was set to be fully wetted, the water flow rate in the anode runner was 0.01 kg/s, and the temperature of the stack was set to different levels at 20 ℃, 40 ℃, 60 ℃, and 80 ℃. By gradually increasing the load current, the relationship between the polarization voltage and the load current density of the PEMEL cell was obtained. As shown in Fig. 8, the electrolyzer polarization voltage gradually increases with the rise of current density, and the increasing rates exhibit significant differences at different current density levels. This observation agrees with the theoretical analysis since the activation polarization losses can vary with current density, affecting the overall voltage change. Furthermore, Fig. 8 shows that although the temperature also affects the PEMEL polarization voltage, the voltage drop is relatively small as the temperature rises due to the small decrease in polarization losses.

Next, Fig. 9 and Fig. 10 compare the simulation results with the experimental data from Weiβ et al. [29] and real-world test data of the demonstration project, respectively. Both Fig. 9 and Fig. 10, the validation experiment is selected under the condition of 60 ℃, and the experimental data match the simulation curves with an error of less than 3 %, which validates the model.

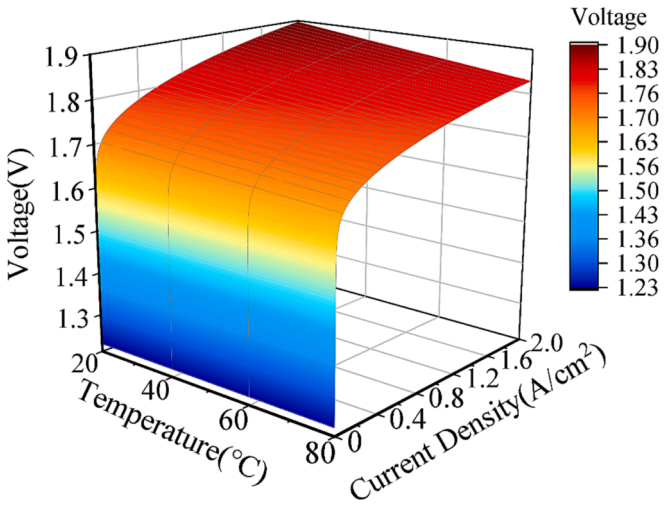

Fig. 8. 3D polarization behavior at different temperatures.

5.1.3. Validation of the HST model

10-h simulations were also carried out to verify the established HST model, where the sampling time is set to one minute. The hydrogen input and output are kept constant and changed twice at 4 h and 5.5 h, respectively. Fig. 11 shows the simulated SOH and hydrogen mass flow rates. From the start of the simulation to 4 h, the HST accumulates hydrogen, and the stored hydrogen reaches the preset upper threshold at the end of this period. Between 4 h and 5.5 h, due to the nearing saturation of the HST and the non-zero input and output of hydrogen gas, the hydrogen storage level experiences continuous fluctuations. The hydrogen's mass flow rates change at 5.5 h, after which the system starts to consume the hydrogen in the HST. The HST reaches the lower limit of hydrogen residual at the approaching 9.5 h. Although the principle states that hydrogen output from the HST should stop after reaching the minimum limit, there is still hydrogen input at the 9.5 h mark. This difference is due to the extended sampling period that allows hydrogen to accumulate between the two sampling points. As a result, the hydrogen release conditions are met at subsequent sampling points,

Fig. 7. Test system: (a) Demonstration project site; (b) 200-kW PEMEL system; (c) 120-kW PEMFC system; (d) Hydrogen storage system.

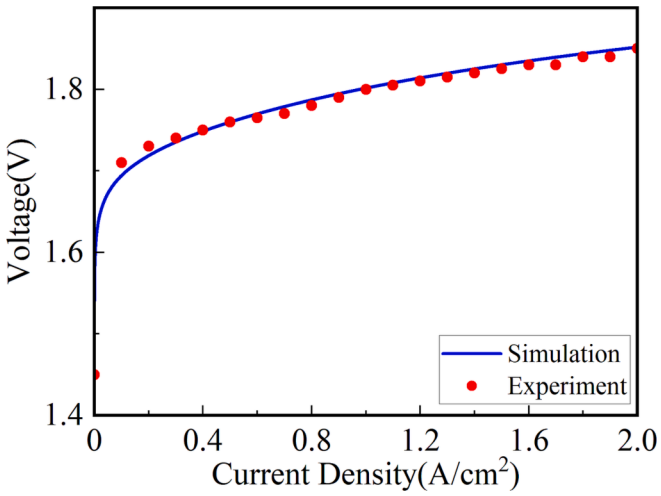

Fig. 9. PEMEL cell polarization curve comparison.

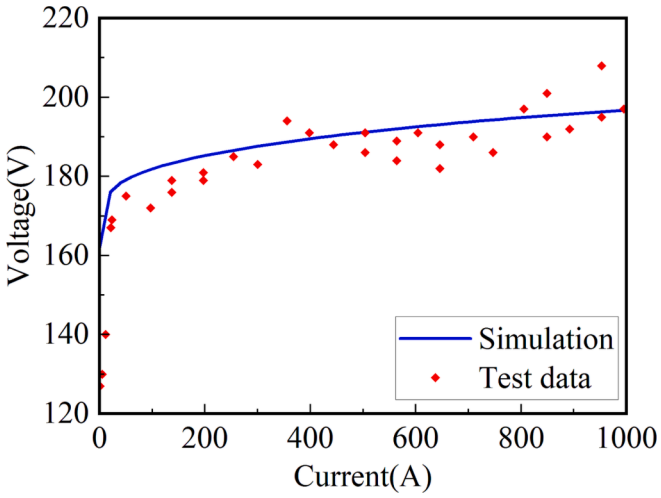

Fig. 10. Volt-ampere characteristics curves of PEMEL stacks comparison.

resulting in a sudden surge in hydrogen output after 9.5 h.

5.1.4. Validation of the PEMFC model

Simulations were conducted to verify the developed PEMFC model. The cathode inlet gas humidity of the PEMFC was set to 100 %, and the membrane was fully wetted. The gas pressure in the cathode runner was set to 2 bar, and the temperature of the stack was set to 20 ℃, 40 ℃, 60 ℃, and 80 ℃, respectively. The load current of the stack was gradually increased, and the relationship between the polarization voltage and the load current density was obtained and shown in Fig. 12.

From Fig. 12, it can be seen that the polarization voltage of the fuel cell exhibits a decreasing trend as the current density increases. Similarly to PEMEL, the decreasing rate of the voltage is different at different current densities. The polarization voltage of the PEMFC decreases as temperature rises, but the corresponding voltage drop is small. It can also be seen from Fig. 12 that at the starting reaction temperature of 60 ℃, the temperature rise of the cell increases with the increasing current density.

To further verify the PEMFC model, the simulated results are compared with the experimental data of Xia et al. [56] in Fig. 13. Furthermore, the measured data from the demonstration project is

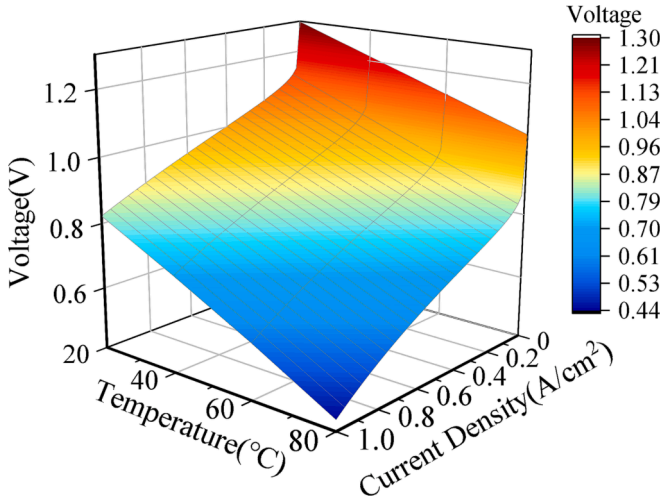

Fig. 12. 3D polarization behavior at different temperatures.

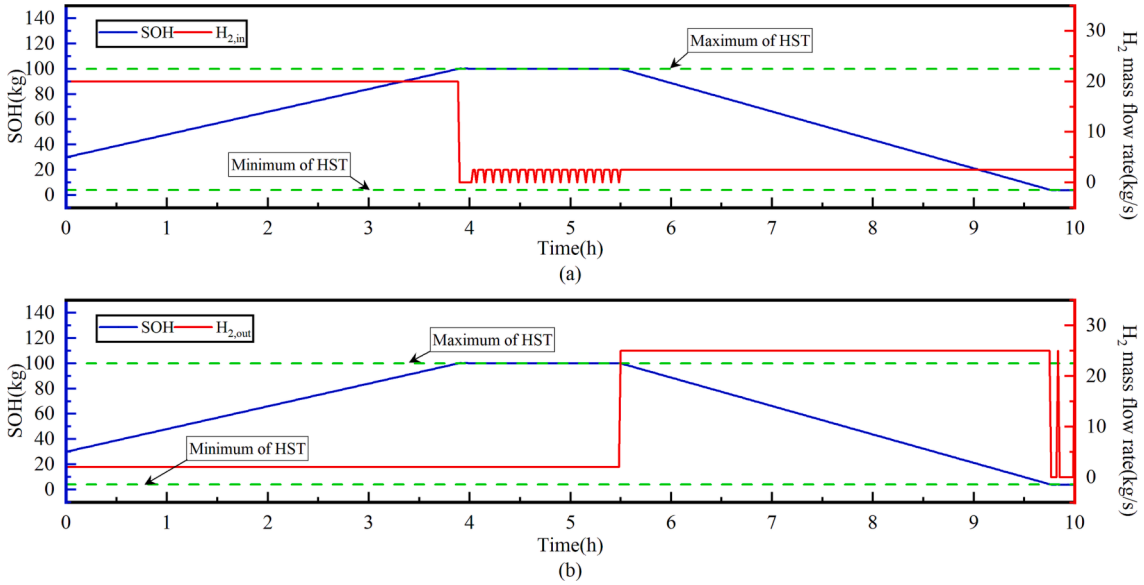

Fig. 11. Hydrogen flow rate and HST real-time hydrogen storage.

compared in Fig. 14. Both Fig. 13 and Fig. 14, the validation experiment is selected under the condition of 60 ℃. It can be seen that the experimental data match the simulation curves with an error of less than 5 %, demonstrating the model's validity.

5.2. Determination of the operation parameters

5.2.1. Main parameters of subsystem

By analyzing the results of the model feasibility analysis obtained in Section 4.1, it is possible to obtain enhanced operating conditions for the subsystems. The initial operating temperature of the PEMEL and PEMFC systems has been set to 60 ℃, while the HST operates at ambient temperature. The PEMFC plays a crucial role in the microgrid, filling in the gaps in electrical power by utilizing the hydrogen generated by the PEMEL. Additionally, it harnesses and repurposes waste heat from the power generation process to fulfill heating demands through an efficient heat recovery mechanism.

In terms of voltage degradation rate, based on the existing studies, the voltage degradation of the PEMEL cell is obtained, as shown in Table 7.

In Table 7, it is assumed that the voltage degradation levels are mutually independent and that all cells within the stack exhibit identical performance. The total voltage degradation level of the PEMEL stack can be expressed as

$$\Delta V_d = \eta_{\mathrm{EL}} \cdot (t_m \cdot V_m + t_l \cdot V_l + t_h \cdot V_h) \tag{36}$$

where t_m, t_l, and t_h are the times for the corresponding operating conditions.

5.2.2. Main parameters of the system

The system performance is evaluated in a scenario under 168-h off-grid operation, in which the renewable power generation data of WT and PV are obtained from the demonstration project. The load data are from seven consecutive days of load data in an industrial park. To better show the advantages of the designed system, three additional sets of comparison experiments are set up, the configuration of which is shown in Table 8.

In Table 8, the synthesized power data refers to smooth power profiles characterized by attributes such as rectangular, triangular, or high-frequency oscillating components. The electrolyzer can operate at high power levels for a long time. Other system operating parameters/limits are given as follows.

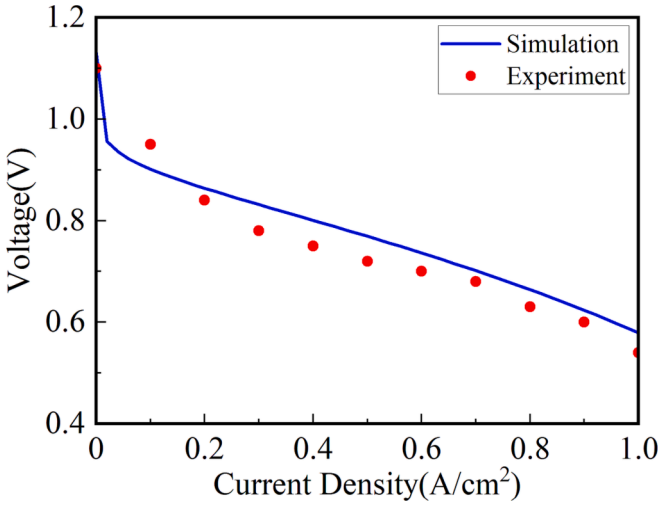

Fig. 13. PEMFC cell polarization curve comparison.

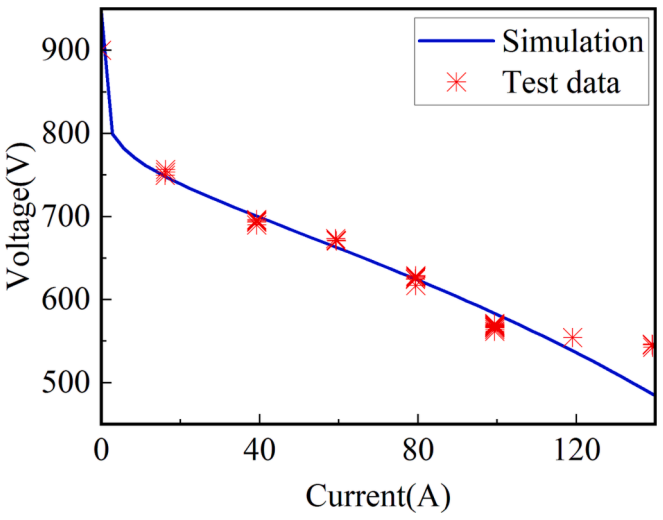

Fig. 14. Volt-ampere characteristics curves of PEMFC stacks comparison.

Table 7
PEMEL cell voltage degradation at different operating conditions.

Operating condition	Parameters	Voltage degradation rate (μV/h)
Maintaining mode	V_m	1.5
Low power fluctuation mode	V_l	50
High power fluctuation mode	V_h	66

Table 8
Operating conditions for simulation.

	Real power data	Synthesized power data	Control strategy
Condition (1)	√	–	√
Condition (2)	√	–	×
Condition (3)	–	√	√
Condition (4)	–	√	×

1) The minimum power for the electrolyzer system start-up is 20 kW, i.e., the rated operating power of auxiliary machines;
2) The shortest time to meet the starting power duration of the electrolyzer is 50 min, and the shortest time to meet the power shortage duration of the electrolyzer is 5 min;
3) The initial hydrogen storage capacity of the HST is 30 kg.

The real power data and the synthesized power profiles are plotted in Fig. 15 and Fig. 16, respectively.

5.3. Evaluation of operating parameters effects

5.3.1. Start/stop signal and aging analysis

Both Fig. 17 and Fig. 18 reveal that the electrolyzer and the fuel cell are running alternately throughout the cycle. The electrolyzer reacts with a slight control delay, and even in some cases, the electrolyzer fails to act while the fuel cell output remains steady. The proposed control strategy mitigates the detrimental impact of frequent starts and stops on the electrolyzer, consequently extending its operational lifespan. The strategy concurrently improves the system's efficiency and cost-effectiveness. In addition, by regulating hydrogen production, the control strategy curtails exhaust gas emissions and resource wastage, leading to a great degree of environmental friendliness.

Next, the time in different operating modes for the four sets of experiments was compared in Fig. 19, where it can be seen that the frequency of PEMEL start-stop is effectively reduced with the proposed control strategy. Fig. 20 shows the degradation of PEMEL in terms of the

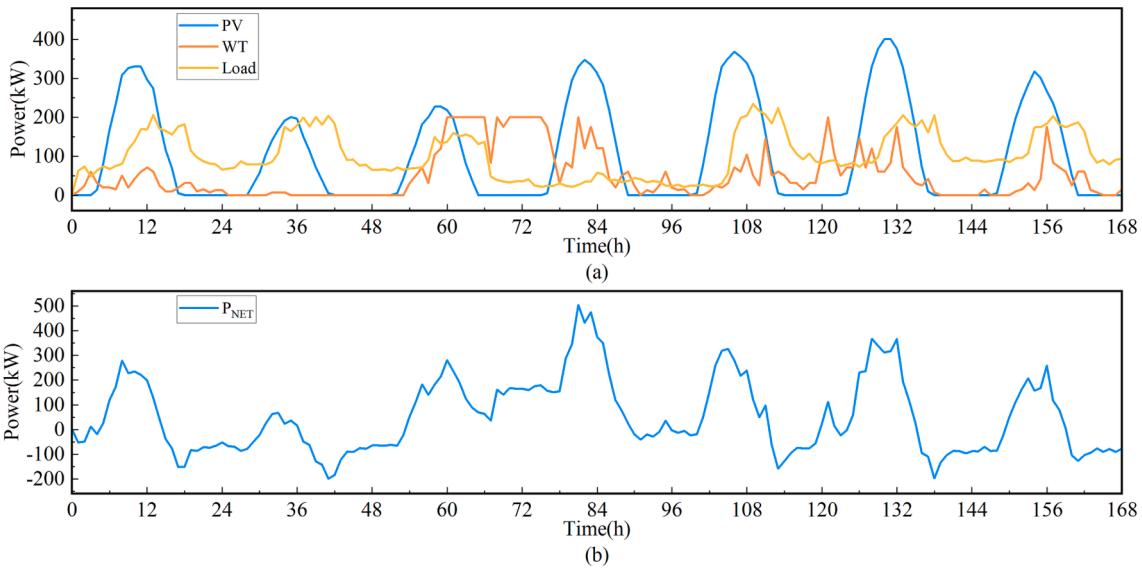

Fig. 15. (a)WT, PV, and load power curves; (b) DC bus net power curve (actual).

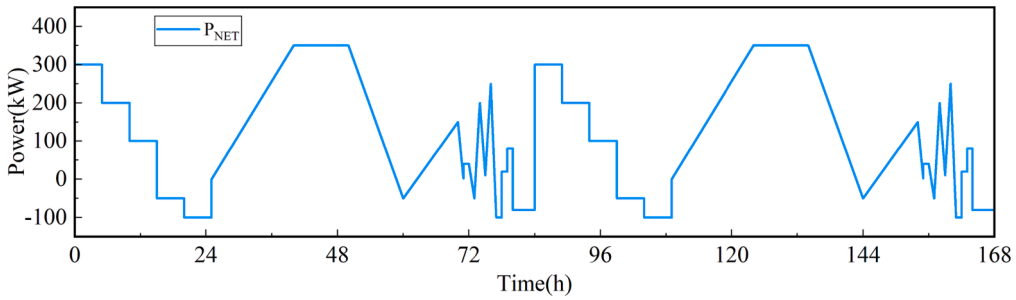

Fig. 16. Synthesized net power curve at the DC bus.

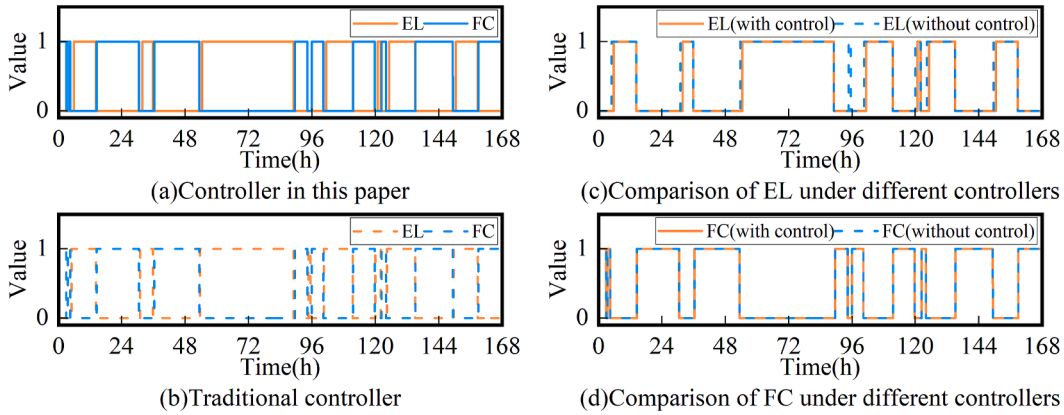

Fig. 17. Start-up Boolean signals for electrolyzer and fuel cell under actual inputs.

voltage drop over time. It can be seen that the voltage decreases from 4.67 mV to 4.48 mV under the condition of real input, while it decreases from 5.40 mV to 5.01 mV under analog input. The voltage degradation rate is significantly suppressed under two different power input conditions, verifying that the PEMEL aging can be effectively refrained with the proposed control strategy.

5.3.2. *Hydrogen and power analysis*

As can be seen from Fig. 21, the hydrogen production is changed because the electrolyzer's working state is changed by the control system. However, as the fuel cell's working state and the hydrogen consumption remain unchanged, the remaining amount of hydrogen in the HST is only related to hydrogen production. The electrolyzer produced 49 kg of hydrogen in one working cycle, and the fuel cell consumed 40 kg of hydrogen.

As seen in Fig. 22, in the presence of the control system, a certain amount of power waste is inevitable in order to alleviate the frequent start and stop of the electrolyzer. Without the control system, the electrolyzer consumed about 14.8 MW of electric power in one cycle. While in the presence of the control system, the electrolyzer only consumed about 14.5 MW of electrical power in one cycle, which wastes about 2 % of the electrical energy. Combining hydrogen production, the calculated

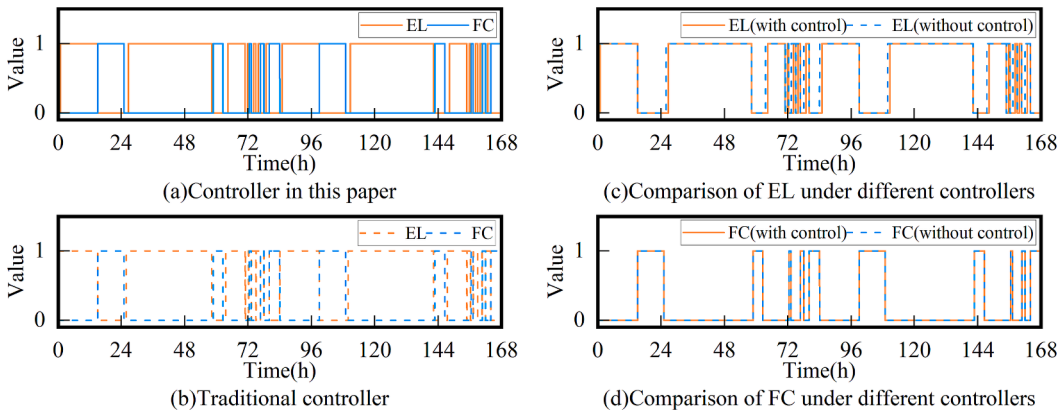

Fig. 18. Start-up Boolean signals for electrolyzer and fuel cell under analog inputs.

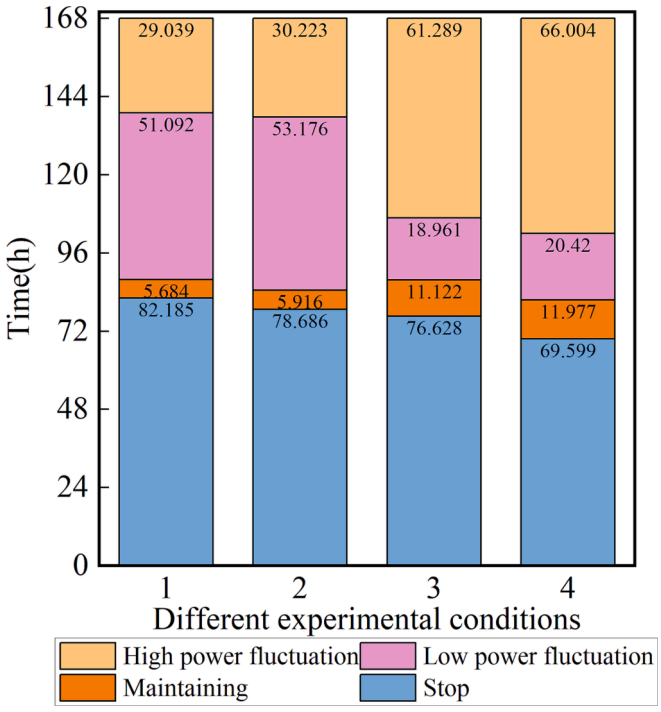

Fig. 19. Working time of PEMEL under different experimental conditions.

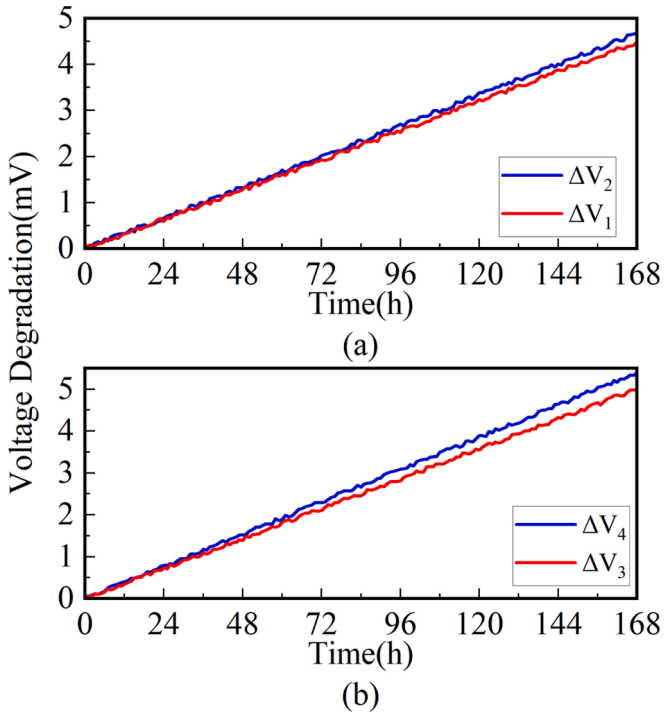

Fig. 20. Voltage degradation of PEMEL in different inputs. (a) Real input. (b) Analog input.

average efficiency of the electrolyzer is 50.8 %.

From Fig. 23, it can be seen that the fuel cell under PID control can adjust its output power according to the load demand. The fuel cell successfully responds to the short-term power demand to ensure the reliable operation of the microgrid. In one cycle, the total power generated by the fuel cell is 6 MW, the hydrogen consumption is 40 kg, and the overall efficiency of the fuel cell can be calculated as 53.6 %.

5.4. Detail exergy analysis for the intergraded system

Based on the voltage and heat production of the PEMFC at different current densities, the exergy destruction and energy efficiency of the fuel cell subsystem under different current conditions are obtained and shown in Fig. 24. It can be seen that for the PEMFC stack, the exergy destruction increases with the increase of stack current, while the exergy efficiency decreases as the stack current increases. As the current increases, the waste heat from the PEMFC also increases, demanding additional cooling water for heat recovery and thus increased exergy destruction to the cooling system.

Fig. 25 shows the cumulative heat recovered (stored as water) by the electrolyzer system over a period of 168 h (simulated input conditions). The system recovers and stores the output heat under the proposed thermal management strategy. The energy utilization of the electrolyzer system increases from 47.6 % to 53.9 %. The efficiency of the electrolyzer is significantly improved.

Fig. 26 shows the cumulative heat recovered (stored as water) by the fuel cell system over a period of 168 h (actual input conditions). The system recovers and stores the output heat with the proposed thermal management strategy. The proposed thermal management strategy significantly increased the energy utilization of the fuel cell system from 53.6 % to 78.1 %.

5.5. Energy flow analysis

Based on the comprehensive analysis presented earlier, a schematic depiction illuminating the energy flow within the system can be derived, as illustrated in Fig. 27. This visual representation unveils that operating

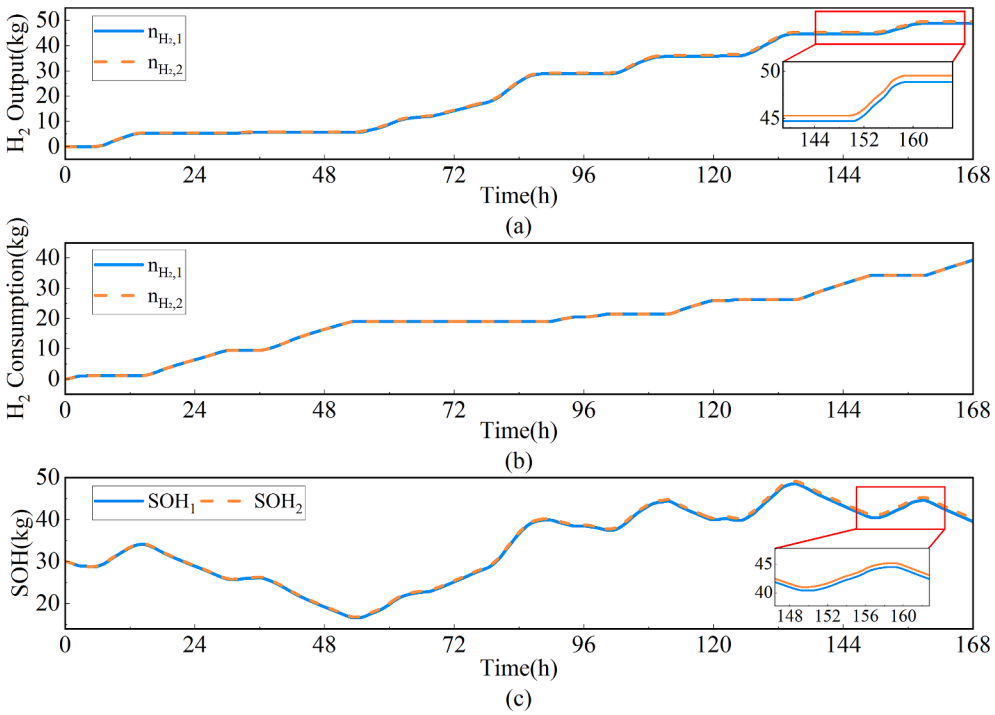

Fig. 21. (a)Hydrogen production rate; (b)Hydrogen consumption rate; (c)SOH in the HST.

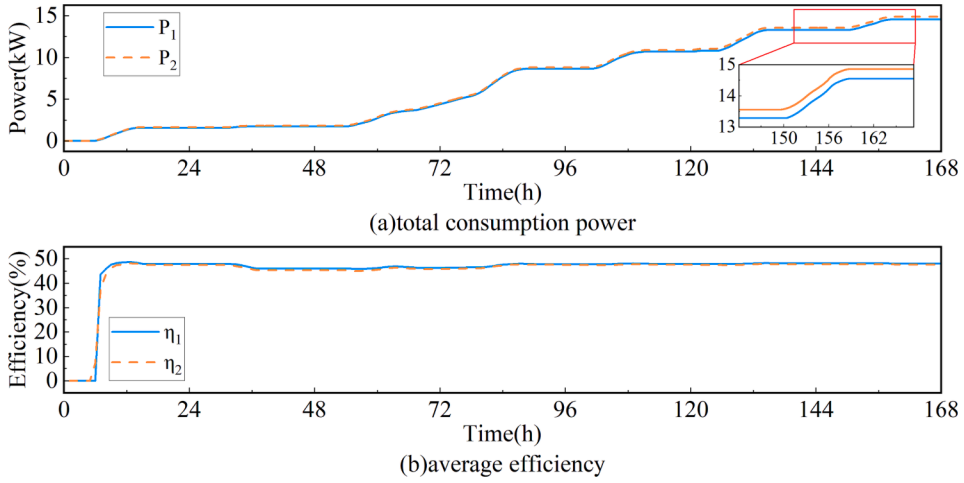

Fig. 22. Electrolyzer power consumption and average efficiency.

under actual input conditions, most of the electricity harvested from the PV and WT caters for the load demand. In particular, the study did not delve into the specific advantages of wind turbines and photovoltaics. The system is designed to conserve energy through the rational distribution of wind and light resources, resulting in inconsistent contributions to wind and light resources as shown in Fig. 27. The residual fraction is fed to the electrolyzer system for hydrogen production. Subsequently, all the hydrogen generated by the electrolyzer is delivered to the HST, and the fuel cell obtains the required hydrogen from the HST to generate electricity to supplement the energy shortage in the load. Furthermore, the heat recovery system captures the heat generated by the fuel cell during the electricity generation to fulfill the heat load requirements. This energy production, storage, and utilization orchestration underscores the system's overarching efficiency and operational efficacy.

6. Conclusion

In this paper, an integrated hydrogen energy utilization system under off-grid operation conditions is proposed. Mathematical models of the system components are established and coupled, and the electrothermal output characteristic curves of the system are obtained. A corresponding energy management strategy is proposed to reduce the unnecessary start and stop of the cell by predicting the input power, which can effectively slow down the aging of the electrolyzer. This strategy improves the energy utilization of the system by recovering the heat produced from different components in the system. Finally, the feasibility of the proposed energy management strategy is verified. The major concluding remarks are given as follows.

1) The proposed strategy ensures that each subsystem can work in its normal operation. The electrolyzer and fuel cell can operate in a way

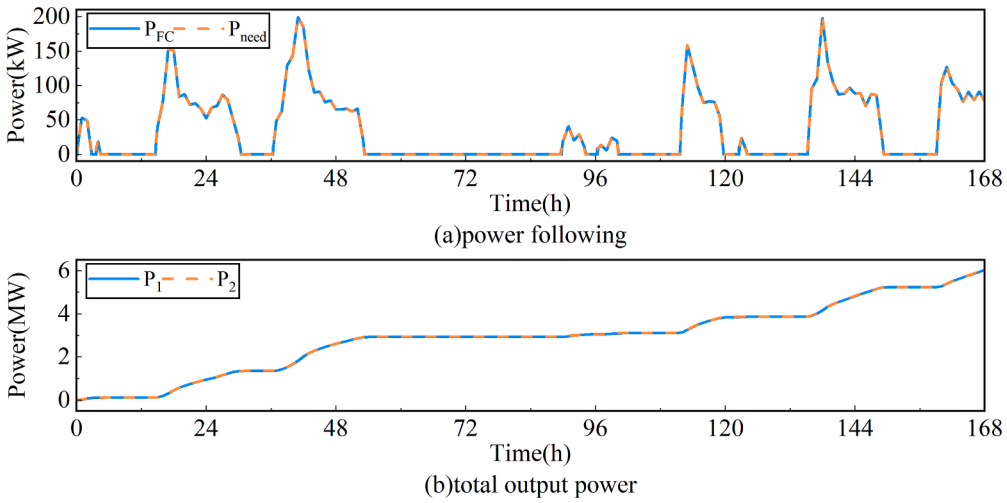

Fig. 23. Power demand and following output power and total fuel cell output power.

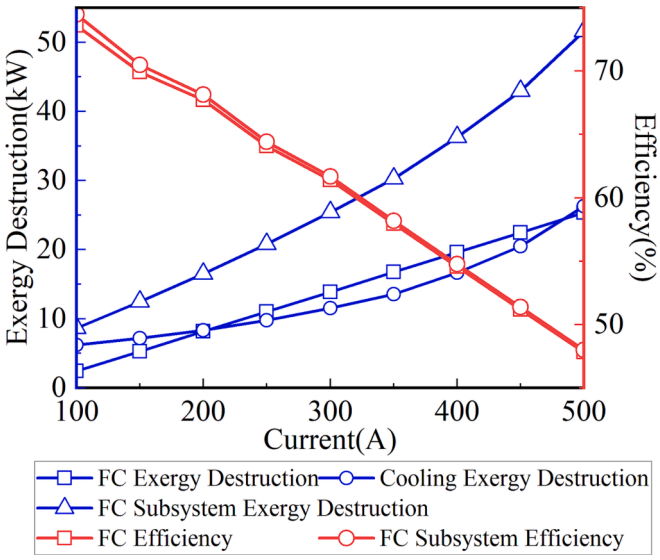

Fig. 24. Exergy destruction and exergy efficiency in the subsystem current variation.

to avoid frequent start-stop, thus extending their service life. The voltage drop of PEMFC is reduced from 4.67 mV to 4.48 mV.

2) The input signal of the fuel cell is controlled through the feedback of the PID controller, which can quickly follow the signal of power shortage of the power grid to achieve the function of timely power compensation. When the sensor detects that the working temperature of the electrolyzer and the fuel cell exceeds the set value, the cooling water cooling system starts to work, exchange heat with the cooling water through the heat exchange plate to maintain the working temperature and send the hot water into the hot water tank to store the heat exchange obtained.
3) The energy efficiency and availability analysis and voltage degradation simulation results show that the proposed control strategy can effectively improve the key performance indicators such as component life and energy efficiency through power allocation and predictive control. The energy efficiencies of the electrolyzer and fuel cell were increased from 47.6 % and 53.6 % to 53.9 % and 78.1 %, respectively, and the service life of the electrolyzer was extended.

It should be noted that the auxiliary device control can be integrated into the proposed control strategy to further improve the system performance. The by-product oxygen produced by hydrogen production in the electrolyzer can be supplied to the fuel cell as fuel. Hydrogen storage

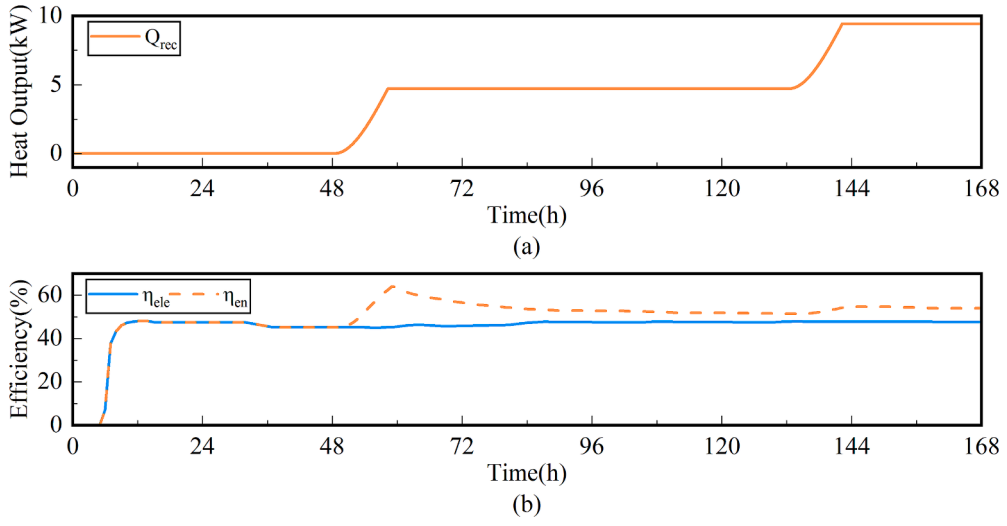

Fig. 25. PEMEL recovered heat and efficiency (a)heat output; (b)electrical and energy efficiency.

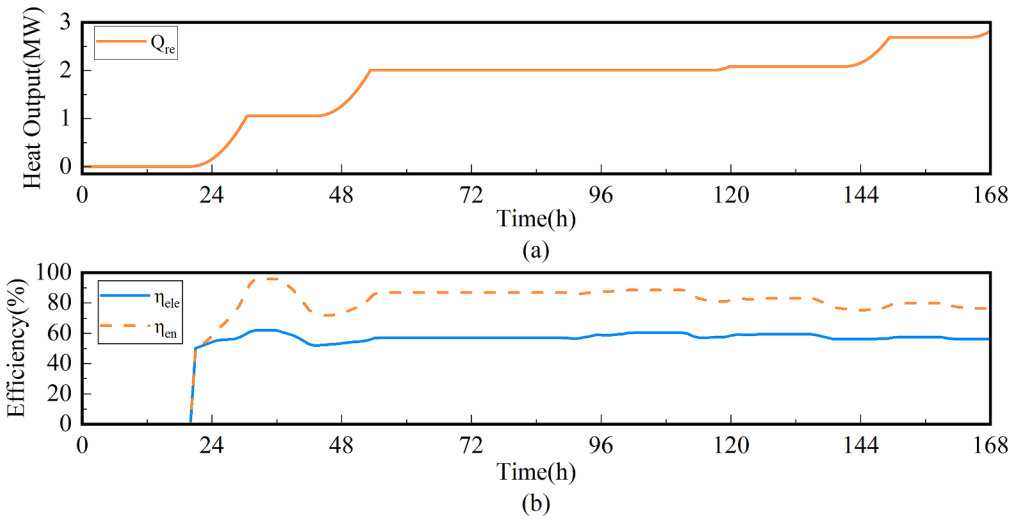

Fig. 26. PEMFC recovered heat and efficiency (a) heat output; (b) electrical and energy efficiency.

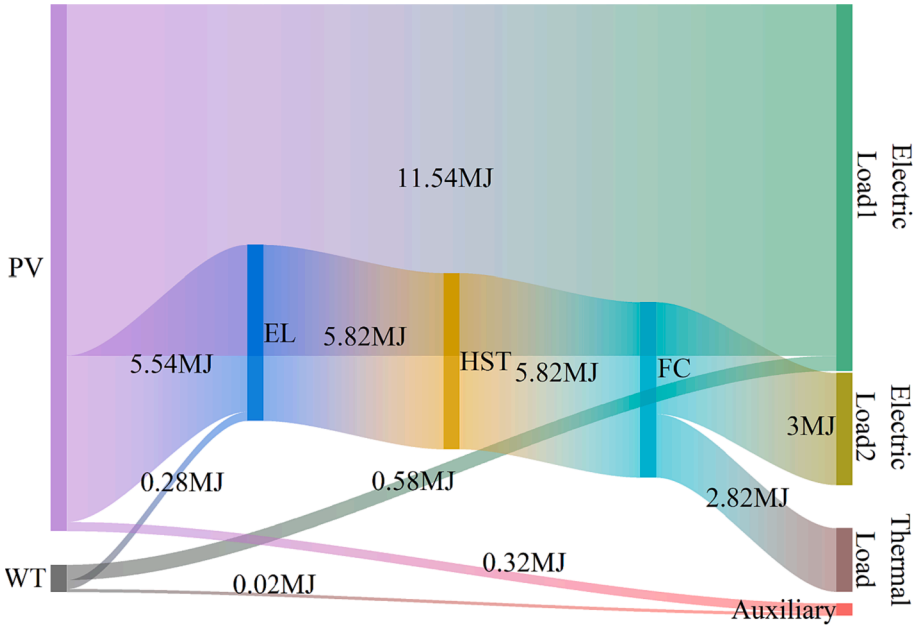

Fig. 27. System energy flow diagram.

can be more economical and reliable. These will be investigated in our future research.

CRediT authorship contribution statement

Banghua Du: Writing – original draft, Methodology, Data curation. **Shihao Zhu:** Writing – original draft, Formal analysis. **Wenchao Zhu:** Investigation, Formal analysis, Software. **Xinyu Lu:** Data curation. **Yang Li:** Writing – review & editing, Validation. **Changjun Xie:** Writing – review & editing, Supervision, Funding acquisition, Conceptualization. **Bo Zhao:** Supervision, Project administration. **Leiqi Zhang:** Methodology, Investigation. **Guizhi Xu:** Validation, Project administration, Funding acquisition. **Jie Song:** Software.

Declaration of Competing Interest

The authors declare that they have no known competing financial interests or personal relationships that could have appeared to influence the work reported in this paper.

Data availability

Data will be made available on request.

Acknowledgment

This paper is supported by the National Key Research and Development Program of China (No. 2020YFB1506802) and the State Grid Corporation of China Technology Program (No. 52110421005H).

References

[1] Elgarahy AM, Hammad A, El-Sherif DM, Abouzid M, Gaballah MS, Elwakeel KZ. Thermochemical conversion strategies of biomass to biofuels, techno-economic and bibliometric analysis: A conceptual review. J Environ Chem Eng 2021;9(6):106503.

[2] Parra D, Valverde L, Pino FJ, Patel MK. A review on the role, cost and value of hydrogen energy systems for deep decarbonisation. Renew Sustain Energy Rev 2019;101:279–94.
[3] Michaelides EE, Nguyen VN, Michaelides DN. The effect of electric vehicle energy storage on the transition to renewable energy. Green Energy and Intelligent Transportation 2023;2(1):100042.
[4] Elgarahy AM, Eloffy MG, Hammad A, Saber AN, El-Sherif DM, Mohsen A, et al. Hydrogen production from wastewater, storage, economy, governance and applications: a review. Environ Chem Lett 2022;20(6):3453–504.
[5] Elwakeel KZ, Elgarahy AM, Alghamdi HM, El-Qelish M. Recycling of catering waste for sequential production of biohydrogen and biomethane; pre-treatments, batch, and continuous mode studies. J Environ Chem Eng 2023;11(5):110955.
[6] Macedo SF, Peyerl D. Prospects and economic feasibility analysis of wind and solar photovoltaic hybrid systems for hydrogen production and storage: A case study of the Brazilian electric power sector. Int J Hydrogen Energy 2022;47(19):10460–73.
[7] Qiu Y, Zeng T, Zhang C, Wang G, Wang Y, Hu Z, et al. Progress and challenges in multi-stack fuel cell system for high power applications: architecture and energy management. Green Energy and Intelligent Transportation 2023;2(2):100068.
[8] Lu X, Du B, Zhou S, Zhu W, Li Y, Yang Y, et al. Optimization of power allocation for wind-hydrogen system multi-stack PEM water electrolyzer considering degradation conditions. Int J Hydrogen Energy 2023;48(15):5850–72.
[9] Arsad AZ, Hannan MA, Al-Shetwi AQ, Mansur M, Muttaqi KM, Dong ZY, et al. Hydrogen energy storage integrated hybrid renewable energy systems: A review analysis for future research directions. Int J Hydrogen Energy 2022;47(39):17285–312.
[10] He W, Abbas Q, Alharthi M, Mohsin M, Hanif I, Vo XV, et al. Integration of renewable hydrogen in light-duty vehicle: nexus between energy security and low carbon emission resources. Int J Hydrogen Energy 2020;45(51):27958–68.
[11] Xiao P, Hu W, Xu X, Liu W, Huang Q, Chen Z. Optimal operation of a wind-electrolytic hydrogen storage system in the electricity/hydrogen markets. Int J Hydrogen Energy 2020;45(46):24412–23.
[12] Wang X, Li B, Wang Y, Lu H, Zhao H, Xue W. A bargaining game-based profit allocation method for the wind-hydrogen-storage combined system. Appl Energy 2022;310:118472.
[13] Li R, Jin X, Yang P, Sun X, Zhu G, Zheng Y, et al. Techno-economic analysis of a wind-photovoltaic-electrolysis-battery hybrid energy system for power and hydrogen generation. Energ Conver Manage 2023;281:116854.
[14] Tan C, Geng S, Zhao Z, Tan Z. Multi time scale operation optimization of EHHGS considering equipment uncertainty and response characteristics. J Clean Prod 2023;382:135106.
[15] Praveenkumar S, Agyekum EB, Ampah JD, Afrane S, Velkin VI, Mehmood U, et al. Techno-economic optimization of PV system for hydrogen production and electric vehicle charging stations under five different climatic conditions in India. Int J Hydrogen Energy 2022;47(90):38087–105.
[16] Shams MH, Niaz H, Na J, Anvari-Moghaddam A, Liu JJ. Machine learning-based utilization of renewable power curtailments under uncertainty by planning of hydrogen systems and battery storages. J Storage Mater 2021;41:103010.
[17] Dong X, Wu J, Xu Z, Liu K, Guan X. Optimal coordination of hydrogen-based integrated energy systems with combination of hydrogen and water storage. Appl Energy 2022;308:118274.
[18] Liu J, Xu Z, Wu J, Liu K, Guan X. Optimal planning of distributed hydrogen-based multi-energy systems. Appl Energy 2021;281:116107.
[19] Babatunde OM, Munda JL, Hamam Y. Off-grid hybrid photovoltaic–micro wind turbine renewable energy system with hydrogen and battery storage: Effects of sun tracking technologies. Energ Conver Manage 2022;255:115335.
[20] Ishaq H, Dincer I. Comparative assessment of renewable energy-based hydrogen production methods. Renew Sustain Energy Rev 2021;135:110192.
[21] Hernández-Gómez Á, Ramirez V, Guilbert D. Investigation of PEM electrolyzer modeling: Electrical domain, efficiency, and specific energy consumption. Int J Hydrogen Energy 2020;45(29):14625–39.
[22] Fan G, Yang B, Guo P, Lin S, Farkoush SG, Afshar N. Comprehensive analysis and multi-objective optimization of a power and hydrogen production system based on a combination of flash-binary geothermal and PEM electrolyzer. Int J Hydrogen Energy 2021;46(68):33718–37.
[23] Ma Z, Witteman L, Wrubel JA, Bender G. A comprehensive modeling method for proton exchange membrane electrolyzer development. Int J Hydrogen Energy 2021;46(34):17627–43.
[24] Pein M, Neumann NC, Venstrom LJ, Vieten J, Roeb M, Sattler C. Two-step thermochemical electrolysis: An approach for green hydrogen production. Int J Hydrogen Energy 2021;46(49):24909–18.
[25] Feng Q, Liu G, Wei B, Zhang Z, Li H, Wang H. A review of proton exchange membrane water electrolysis on degradation mechanisms and mitigation strategies. J Power Sources 2017;366:33–55.
[26] Khatib FN, Wilberforce T, Ijaodola O, Ogungbemi E, El-Hassan Z, Durrant A, et al. Material degradation of components in polymer electrolyte membrane (PEM) electrolytic cell and mitigation mechanisms: A review. Renew Sustain Energy Rev 2019;111:1–14.
[27] Chandesris M, Médeau V, Guillet N, Chelghoum S, Thoby D, Fouda-Onana F. Membrane degradation in PEM water electrolyzer: Numerical modeling and experimental evidence of the influence of temperature and current density. Int J Hydrogen Energy 2015;40(3):1353–66.
[28] Frensch SH, Fouda-Onana F, Serre G, Thoby D, Araya SS, Kær SK. Influence of the operation mode on PEM water electrolysis degradation. Int J Hydrogen Energy 2019;44(57):29889–98.
[29] Weiß A, Siebel A, Bernt M, Shen TH, Tileli V, Gasteiger HA. Impact of intermittent operation on lifetime and performance of a PEM water electrolyzer. J Electrochem Soc 2019;166(8):F487–97.
[30] Hartig-Weiß A, Bernt M, Siebel A, Gasteiger HA. A Platinum Micro-Reference Electrode for Impedance Measurements in a PEM Water Electrolysis Cell. J Electrochem Soc 2021;168(11):114511.
[31] Abdel-Rehim AA. The influence of electromagnetic field on the performance and operation of a PEM fuel cell stack subjected to a relatively low electromagnetic field intensity. Energ Conver Manage 2019;198:111906.
[32] Niroumand AM, Homayouni H, Goransson G, Olfert M, Eikerling M. In-situ diagnostic tools for hydrogen transfer leak characterization in PEM fuel cell stacks part III: Manufacturing applications. J Power Sources 2020;448:227359.
[33] Li Q, Yin L, Yang H, Wang T, Qiu Y, Chen W. Multiobjective optimization and data-driven constraint adaptive predictive control for efficient and stable operation of PEMFC system. IEEE Trans Ind Electron 2020;68(12):12418–29.
[34] Li Q, Liu P, Meng X, Zhang G, Ai Y, Chen W. Model prediction control-based energy management combining self-trending prediction and subset-searching algorithm for hydrogen electric multiple unit train. IEEE Trans Transp Electrif 2022;8(2):2249–60.
[35] Li Q, Cai L, Yin L, Wang T, Li L, **e, S., & Chen, W.. An energy management strategy considering the economy and lifetime of multi-stack fuel cell hybrid system. IEEE Trans Transp Electrif 2022.
[36] Naseri, N., El Hani, S., Aghmadi, A., Mediouni, H., Aboudrar, I., & Benbouzid, M. (2019, October). Solar photovoltaic energy storage as hydrogen via PEM fuel cell for later conversion back to electricity. In IECON 2019-45th Annual Conference of the IEEE Industrial Electronics Society (Vol. 1, pp. 4549-4554). IEEE.
[37] Xu, M., Zhang, G., Li, W., Ge, L., Song, Z., Geng, Y., & Wang, J. (2019, October). Coordinated control strategy for grid-connected integrated energy system of wind, photovoltaic and hydrogen. In 2019 IEEE 8th International Conference on Advanced Power System Automation and Protection (APAP) (pp. 1120-1124). IEEE.
[38] Nafeh AESA. Hydrogen production from a PV/PEM electrolyzer system using a neural-network-based MPPT algorithm. Int J Numer Model Electron Networks Devices Fields 2011;24(3):282–97.
[39] Nafchi FM, Afshari E, Baniasadi E, Javani N. A parametric study of polymer membrane electrolyser performance, energy and exergy analyses. Int J Hydrogen Energy 2019;44(34):18662–70.
[40] Görgün H. Dynamic modelling of a proton exchange membrane (PEM) electrolyzer. Int J Hydrogen Energy 2006;31(1):29–38.
[41] Hug W, Bussmann H, Brinner A. Intermittent operation and operation modeling of an alkaline electrolyzer. Int J Hydrogen Energy 1993;18(12):973–7.
[42] Ulleberg Ø. Modeling of advanced alkaline electrolyzers: a system simulation approach. Int J Hydrogen Energy 2003;28(1):21–33.
[43] Tiktak WJ. Heat Management of PEM Electrolysis. CD Delft, The Netherlands: Delft University of Technology; 2019.
[44] Olivier P, Bourasseau C, Bouamama PB. Low-temperature electrolysis system modelling: A review. Renew Sustain Energy Rev 2017;78:280–300.
[45] Kothandaraman CP. Fundamentals of heat and mass transfer. New Age 2006. International.
[46] Pathapati PR, Xue X, Tang J. A new dynamic model for predicting transient phenomena in a PEM fuel cell system. Renew Energy 2005;30(1):1–22.
[47] Corrêa JM, Farret FA, Canha LN, Simoes MG. An electrochemical-based fuel-cell model suitable for electrical engineering automation approach. IEEE Trans Ind Electron 2004;51(5):1103–12.
[48] Springer TE, Zawodzinski TA, Gottesfeld S. Polymer electrolyte fuel cell model. J Electrochem Soc 1991;138(8):2334.
[49] Kim J, Lee SM, Srinivasan S, Chamberlin CE. Modeling of proton exchange membrane fuel cell performance with an empirical equation. J Electrochem Soc 1995;142(8):2670.
[50] Liso V, Nielsen MP, Kær SK, Mortensen HH. Thermal modeling and temperature control of a PEM fuel cell system for forklift applications. Int J Hydrogen Energy 2014;39(16):8410–20.
[51] Matute G, Yusta JM, Beyza J, Correas LC. Multi-state techno-economic model for optimal dispatch of grid connected hydrogen electrolysis systems operating under dynamic conditions. Int J Hydrogen Energy 2021;46(2):1449–60.
[52] Niu D, Sun L, Yu M, Wang K. Point and interval forecasting of ultra-short-term wind power based on a data-driven method and hybrid deep learning model. Energy 2022;254:124384.
[53] Mahon H, O'Connor D, Friedrich D, Hughes B. A review of thermal energy storage technologies for seasonal loops. Energy 2022;239:122207.
[54] Babic U, Suermann M, Büchi FN, Gubler L, Schmidt TJ. Critical review—identifying critical gaps for polymer electrolyte water electrolysis development. J Electrochem Soc 2017;164(4):F387.
[55] Lu X, Du B, Zhu W, Yang Y, Xie C, Tu Z, et al. Thermodynamic and dynamic analysis of a hybrid PEMFC-ORC combined heat and power (CHP) system. Energ Conver Manage 2023;292:117408.
[56] Xia S, Lin R, Cui X, Shan J. The application of orthogonal test method in the parameters optimization of PEMFC under steady working condition. Int J Hydrogen Energy 2016;41(26):11380–90.